



# The Kangaroo's First Hop: The Early Fast Cooling Phase of EP250108a/SN 2025kg

Rob A. J. Eyles-Ferris<sup>1</sup>, Peter G. Jonker<sup>2</sup>, Andrew J. Levan<sup>2</sup>, Daniele Bjørn Malesani<sup>3,4</sup>, Nikhil Sarin<sup>5,6</sup>, Christopher L. Fryer<sup>7</sup>, Jillian C. Rastinejad<sup>8</sup>, Eric Burns<sup>9</sup>, Nial R. Tanvir<sup>1</sup>, Paul T. O'Brien<sup>1</sup>, Wen-fai Fong<sup>8</sup>, Ilya Mandel<sup>10,11</sup>, Benjamin P. Gompertz<sup>12,13</sup>, Charles D. Kilpatrick<sup>8</sup>, Steven Bloemen<sup>2</sup>, Joe S. Bright<sup>14</sup>, Francesco Carotenuto<sup>15</sup>, Gregory Corcoran<sup>16</sup>, Laura Cotter<sup>16</sup>, Paul J. Groot<sup>2,17,18</sup>, Luca Izzo<sup>4,19</sup>, Tanmoy Laskar<sup>20,21</sup>, Antonio Martin-Carrillo<sup>16</sup>, Jesse Palmerio<sup>22</sup>, Maria E. Ravasio<sup>2,23</sup>, Jan van Roestel<sup>24</sup>, Andrea Saccardi<sup>22</sup>, Rhaana L. C. Starling<sup>1</sup>, Aishwarya Linesh Thakur<sup>25</sup>, Susanna D. Vergani<sup>23,26</sup>, Paul M. Vreeswijk<sup>2</sup>, Franz E. Bauer<sup>27</sup>, Sergio Campana<sup>23</sup>, Jennifer A. Chacón<sup>28,29</sup>, Ashley A. Chrimes<sup>2,30</sup>, Stefano Covino<sup>23,31</sup>, Joyce N. D. van Dalen<sup>2</sup>, Valerio D'Elia<sup>32</sup>, Massimiliano De Pasquale<sup>33</sup>, Nusrin Habeeb<sup>1</sup>, Dieter H. Hartmann<sup>34</sup>, Agnes P. C. van Hoof<sup>2</sup>, Páll Jakobsson<sup>35</sup>, Yashaswi Julakanti<sup>1</sup>, Giorgos Leloudas<sup>36</sup>, Daniel Mata Sánchez<sup>37,38</sup>, Christopher J. Nixon<sup>39</sup>, Daniëlle L. A. Pieterse<sup>2</sup>, Giovanna Pugliese<sup>40</sup>, Jonathan Quirola-Vásquez<sup>2</sup>, Ben C. Rayson<sup>1</sup>, Ruben Salvaterra<sup>41</sup>, Ben Schneider<sup>42</sup>, Manuel A. P. Torres<sup>37,38</sup>, and Tayyaba Zafar<sup>43</sup>

<sup>1</sup> School of Physics and Astronomy, University of Leicester, University Road, Leicester LE1 7RH, UK; [raje1@leicester.ac.uk](mailto:raje1@leicester.ac.uk)

<sup>2</sup> Department of Astrophysics/IMAPP, Radboud University, P.O. Box 9010, 6500 GL, Nijmegen, The Netherlands

<sup>3</sup> Cosmic Dawn Center (DAWN), Denmark

<sup>4</sup> Niels Bohr Institute, University of Copenhagen, Jagtvej 128, Copenhagen 2200, Denmark

<sup>5</sup> The Oskar Klein Centre, Department of Physics, Stockholm University, AlbaNova, Stockholm, SE-106 91 Stockholm, Sweden

<sup>6</sup> Nordita, Stockholm University and KTH Royal Institute of Technology, Hannes Alfvéns väg 12, Stockholm, SE-106 91 Stockholm, Sweden

<sup>7</sup> Center for Nonlinear Studies, Los Alamos National Laboratory, Los Alamos, NM 87545, USA

<sup>8</sup> Center for Interdisciplinary Exploration and Research in Astrophysics (CIERA) and Department of Physics and Astronomy, Northwestern University, Evanston, IL 60208, USA

<sup>9</sup> Department of Physics and Astronomy, Louisiana State University, Baton Rouge, LA 70803, USA

<sup>10</sup> School of Physics and Astronomy, Monash University, Clayton, VIC 3800, Australia

<sup>11</sup> ARC Centre of Excellence for Gravitational-wave Discovery (OzGrav), Melbourne, Australia

<sup>12</sup> School of Physics and Astronomy, University of Birmingham, Birmingham B15 2TT, UK

<sup>13</sup> Institute for Gravitational Wave Astronomy, University of Birmingham, Birmingham B15 2TT, UK

<sup>14</sup> Astrophysics, Department of Physics, University of Oxford, Keble Road, Oxford OX1 3RH, UK

<sup>15</sup> INAF-Osservatorio Astronomico di Roma, Via Frascati 33, I-00078 Monte Porzio Catone (RM), Italy

<sup>16</sup> School of Physics and Centre for Space Research, University College Dublin, Belfield, Dublin 4, Ireland

<sup>17</sup> Department of Astronomy, University of Cape Town, Private Bag X3, Rondebosch 7701, South Africa

<sup>18</sup> South African Astronomical Observatory, P.O. Box 9, Observatory 7935, South Africa

<sup>19</sup> Osservatorio Astronomico di Capodimonte, INAF, Salita Moiriello 16, Napoli, 80131, Italy

<sup>20</sup> Department of Physics & Astronomy, University of Utah, Salt Lake City, UT 84112, USA

<sup>21</sup> Department of Astrophysics/IMAPP, Radboud University, PO Box 9010, 6500 GL Nijmegen, The Netherlands

<sup>22</sup> Université Paris-Saclay, Université Paris Cité, CEA, CNRS, AIM, 91191 Gif-sur-Yvette, France

<sup>23</sup> INAF—Osservatorio Astronomico di Brera, Via E. Bianchi 46, I-23807 Merate, (LC), Italy

<sup>24</sup> Anton Pannekoek Institute for Astronomy, University of Amsterdam, 1090 GE Amsterdam, The Netherlands

<sup>25</sup> INAF—Istituto di Astrofisica e Planetologia Spaziali, Via Fosso del Cavaliere 100, 00133 Roma, Italy

<sup>26</sup> GEPI, Observatoire de Paris, Université PSL, CNRS, 5 Place Jules Janssen, F-92190 Meudon, France

<sup>27</sup> Instituto de Alta Investigación, Universidad de Tarapacá, Casilla 7D, Arica, Chile

<sup>28</sup> Instituto de Astrofísica, Facultad de Física, Pontificia Universidad Católica de Chile, Campus San Joaquín, Av. Vicuña Mackenna 4860, Macul Santiago 7820436, Chile

<sup>29</sup> Millennium Institute of Astrophysics, Nuncio Monseñor Sótero Sanz 100, 104 Providencia, Santiago, Chile

<sup>30</sup> European Space Agency (ESA), European Space Research and Technology Centre (ESTEC), Keplerlaan 1, 2201 AZ Noordwijk, The Netherlands

<sup>31</sup> Como Lake Centre for AstroPhysics (CLAP), DiSAT, Università dell'Insubria, Via Valleggio 11, 22100 Como, Italy

<sup>32</sup> Space Science Data Center (SSDC)—Agenzia Spaziale Italiana (ASI), I-00133 Roma, Italy

<sup>33</sup> Department of Mathematics and Computer Sciences, Physical Sciences and Earth Sciences, University of Messina, Via F. S. D'Alcontres 31, 98166 Messina, Italy

<sup>34</sup> Department of Physics and Astronomy, Clemson University, Clemson, SC 29634-0978, USA

<sup>35</sup> Center for Astrophysics and Cosmology, Science Institute, University of Iceland, Dunhagi 5, 107 Reykjavík, Iceland

<sup>36</sup> DTU Space, National Space Institute, Technical University of Denmark, Elektrovej 327, 2800 Kgs. Lyngby, Denmark

<sup>37</sup> Instituto de Astrofísica de Canarias, E-38205 La Laguna, Tenerife, Spain

<sup>38</sup> Departamento de Astrofísica, University de La Laguna, E-38206 La Laguna, Tenerife, Spain

<sup>39</sup> School of Physics and Astronomy, Sir William Henry Bragg Building, University of Leeds, Woodhouse Ln., Leeds LS2 9JT, UK

<sup>40</sup> Astronomical Institute Anton Pannekoek, University of Amsterdam, 1090 GE Amsterdam, The Netherlands

<sup>41</sup> INAF—Istituto di Astrofisica Spaziale e Fisica Cosmica di Milano, Via A. Corti 12, 20133 Milano, Italy

<sup>42</sup> Aix Marseille University, CNRS, CNES, LAM, Marseille, France

<sup>43</sup> School of Mathematical and Physical Sciences, Macquarie University, NSW 2109, Australia

Received 2025 April 11; revised 2025 May 17; accepted 2025 June 4; published 2025 July 16



Original content from this work may be used under the terms of the [Creative Commons Attribution 4.0 licence](https://creativecommons.org/licenses/by/4.0/). Any further distribution of this work must maintain attribution to the author(s) and the title of the work, journal citation and DOI.

## Abstract

Fast X-ray transients are a rare and poorly understood population of events. Previously difficult to detect in real time, the launch of the Einstein Probe with its Wide-field X-ray Telescope has led to a rapid expansion of the sample and allowed the exploration of these transients across the electromagnetic spectrum. EP250108a is a recently detected example linked to an optical counterpart, SN 2025kg, or “the kangaroo.” Together with a companion Letter we present our observing campaign and analysis of this event. In this letter, we focus on the early evolution of the optical counterpart over the first 6 days, including our measurement of the redshift of  $z = 0.17641$ . We compare to other supernovae and fast transients showing similar features, finding significant similarities with SN 2006aj and SN 2020bvc, and show that the source is well modelled by a rapidly expanding cooling blackbody. We show the observed X-ray and radio properties are consistent with a collapsar-powered jet that is low energy ( $\lesssim 10^{51}$  erg) and/or fails to break out of the dense material surrounding it. While we examine the possibility that the optical emission emerges from the shock produced as the supernova ejecta expand into a dense shell of circumstellar material, due to our X-ray and radio inferences, we favour a model where it arises from a shocked cocoon resulting from a trapped jet. This makes SN 2025 one of the few examples of this currently observationally rare event.

*Unified Astronomy Thesaurus concepts:* X-ray transient sources (1852); High energy astrophysics (739); Type Ic supernovae (1730); Gamma-ray bursts (629)

## 1. Introduction

The Einstein Probe (hereafter EP; W. Yuan et al. 2022), launched just over a year ago, and has already made significant contributions to the field of high-energy X-ray astronomy. In particular, it has vastly increased the known sample of fast X-ray transients (FXTs) with its Wide-field X-ray Telescope (WXT).

FXTs are outbursts detected in the soft X-ray regime (typically  $< 10$  keV), and are characterized by timescales of tens to thousands of seconds. While they were found in early sounding rocket experiments, until recently, meaningful samples have been identified in targeted searches of archival data (e.g., P. G. Jonker et al. 2013; A. Glennie et al. 2015; F. E. Bauer et al. 2017; D. Alp & J. Larsson 2020; A. De Luca et al. 2021; J. Quirola-Vásquez et al. 2022, 2023). While there are exceptions to this rule, such as the fortuitous detection of the X-ray flare that accompanied the Type Ib supernova SN 2008D (e.g., P. A. Mazzali et al. 2008; A. M. Soderberg et al. 2008; D. Malesani et al. 2009; M. Modjaz et al. 2009), these have historically been extremely rare. However, in only a year of operations, EP/WXT has detected  $\sim 100$  FXTs and vastly increased the observed sample of these rare transients. These FXTs have been detected and communicated to the community in near real time and allowed in depth analysis of many of their counterparts across the electromagnetic spectrum.

The properties of the FXTs detected by EP are diverse and likely represent a wide range of transient types and progenitor systems. While the nature and origins of many remain mysterious (e.g., B. O’Connor et al. 2025; W. Zhang et al. 2025), several have been linked to the core collapse of massive stars. Both EP240219a and EP240315a, for instance, were linked to collapsar-driven long gamma-ray bursts (GRBs; e.g., A. J. Levan et al. 2024; Y.-H. I. Yin et al. 2024; Y. Liu et al. 2025b). In these particular cases, the FXT is likely the lower-energy counterpart of internal shocks in a powerful relativistic jet produced by the cataclysmic collapse of these stars. Other EP FXTs have also been seen to be linked to Type Ic supernovae (H. Sun et al. 2025; S. Srivastav et al. 2025; J. N. D. van Dalen et al. 2025), which are known to be produced by similar progenitors as long GRBs and are often observed following such an event (e.g., S. E. Woosley et al. 1999; S. E. Woosley & J. S. Bloom 2006; C. Georgy et al. 2009; M. Modjaz et al. 2016).

However, the sources linked to FXTs have often proven to be unusual when compared to the respective populations of these

events as observed by other facilities. For example, EP240315a was shown to exhibit soft X-ray emission hundreds of seconds earlier and for far longer than the gamma-ray emission (Y. Liu et al. 2025b), suggesting significant central engine activity outside the window suggested by the gamma rays. As another example, SN 2024gsa, the Type Ic supernova linked to EP240414a, was accompanied by two distinct thermal emission episodes between the FXT detection and the rise of the supernova suggesting a link to fast blue optical transients (FBOTs; H. Sun et al. 2025; S. Srivastav et al. 2025; J. N. D. van Dalen et al. 2025).

FBOTs are fast evolving and bright at UV and optical wavelengths. Similarly to the term FXT, FBOT indicates a phenomenological rather than physical description and the observed population is therefore diverse. Several subclasses, such as luminous FBOTs (LFBOTs; e.g., D. A. Perley et al. 2019, 2021; D. L. Coppejans et al. 2020; J. S. Bright et al. 2022; A. Y. Q. Ho et al. 2022a; C. P. Gutiérrez et al. 2024), have been identified and the differing natures of these classes implies FBOTs arise from a variety of systems and progenitors. EP240414a/SN 2024gsa implies the existence of systems where weak jets fail to efficiently break out of a dense stellar envelope or circumstellar medium (CSM). Rather than producing a long GRB, the resulting shocked material produces a blue thermal component providing an origin for some FBOTs.

In this letter, we present our observations and analysis of the early evolution of a unique FXT, EP250108a, detected by EP/WXT on 2025 January 8 (R. Z. Li et al. 2025a), and which allows us to probe the origin of these enigmatic transients. While this event was reported some 18 hr after the detection and further X-ray observations identified no continued emission (R. Z. Li et al. 2025b), our rapid optical follow-up identified a counterpart (R. A. J. Eyles-Ferris 2025) and prompting multiwavelength observations by the community. EP250108a’s optical counterpart was quickly found to be unusual with a spectral energy distribution (SED) consistent with a hot thermal source (D. B. Malesani et al. 2025; Z. P. Zhu et al. 2025a, 2025b) characteristic of an FBOT, tidal disruption event, or supernova rather than a power law as is typical for a GRB afterglow. This behavior is similar to that exhibited by SN 2024gsa, the first EP FXT supernova, or that of (L)FBOTs. Based on its initial moniker of AT2025kg, EP250108a’s optical counterpart was dubbed “the kangaroo.” The thermal source rapidly faded before starting to rebrighten  $\sim 7$  days postdetection (R. A. J. Eyles-Ferris et al. 2025;

F. F. Song et al. 2025). Spectroscopic observations showed the rebrightening to be a rising Type Ic broad lined (Ic-BL) supernova (A. J. Levan et al. 2025b; D. Xu et al. 2025) and the optical source became SN 2025kg, which we explore in further detail in J. C. Rastinejad et al. (2025). Notably, at its redshift of  $z=0.17641$  (see below), SN 2025kg is the currently the closest EP FXT with a supernova connection.

Here we present the early evolution of EP250108a/SN 2025kg covering the first 5 days (observer frame) post-EP/WXT detection, hereafter referred to as the fast cooling phase. We also include X-ray and radio data covering the first 20 and 43 days, respectively, which we use to inform our analysis of the presence of a jet. The later UV–optical–IR (UVOIR) evolution of the source, particularly the Ic-BL supernova, is explored in a companion Letter (J. C. Rastinejad et al. 2025).

EP250108a/SN 2025kg is a valuable opportunity that has been seized by several groups in the community, in particular G. P. Srinivasaragavan et al. (2025) and W. X. Li et al. (2025). We also compare our results to these papers where appropriate.

Throughout this letter, we adopt a Planck cosmology (Planck Collaboration et al. 2020). At SN 2025kg’s redshift of  $z=0.17641$ , this corresponds to a luminosity distance of 880.6 Mpc. Throughout this work, errors are given to  $1\sigma$ .

## 2. Observations and Data Reduction

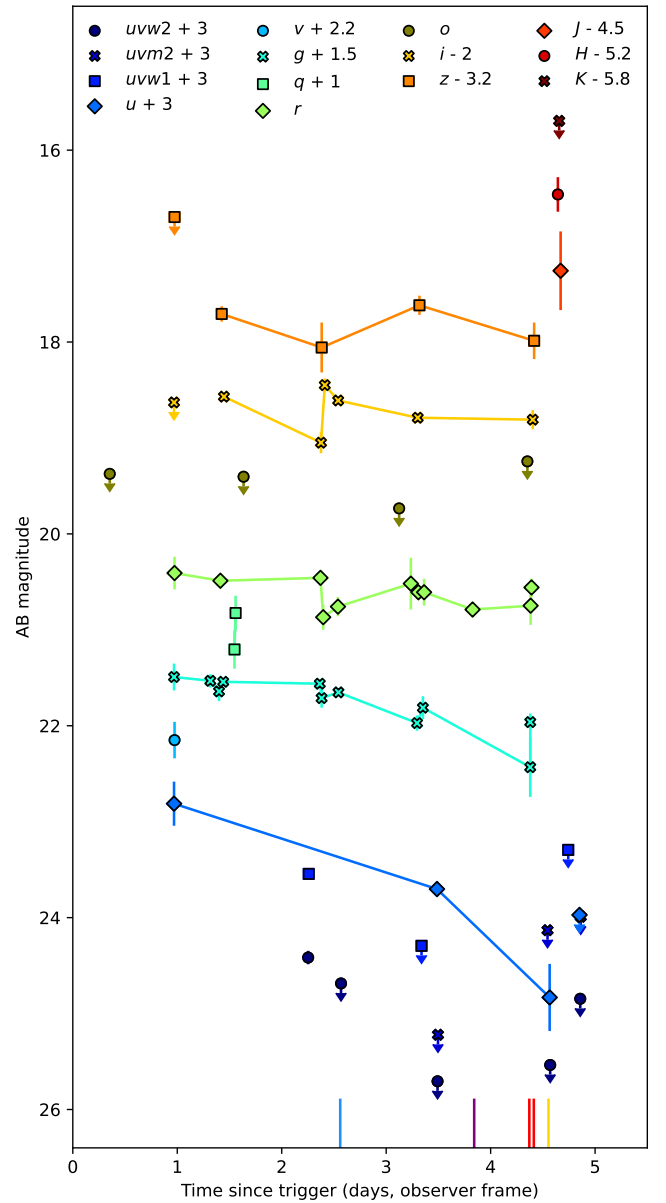
Our observing campaign for SN 2025kg has been extensive in terms of both time and wavelength coverage. In this section, we summarize the observations taken during the fast cooling phase and their reduction.

### 2.1. Ultraviolet, Optical, and Near-infrared

#### 2.1.1. Photometry

During the fast cooling phase, we obtained photometric observations with seven telescopes with a total exposure time in excess of 20 ks. We present our assembled photometry for the fast cooling phase of SN 2025kg in Appendix A, also including the photometry reported in GCN Circulars, and show the complete light curve in Figure 1. In our analysis, we correct our photometry for a Milky Way extinction of  $A_V = 0.049$  (E. F. Schlafly & D. P. Finkbeiner 2011) using the `dust_extinction v1.5` package (K. Gordon 2024) and the K. D. Gordon et al. (2023; see also K. D. Gordon et al. 2009, 2021; E. L. Fitzpatrick et al. 2019; M. Declair et al. 2022) Milky Way model with  $R_V = 3.1$ .

Following the detection of EP250108a, observations were initiated with the 2 m Liverpool Telescope (LT; I. A. Steele et al. 2004) using the IO:O instrument (Program IDs PL24B06 and PL25A25; PI: Eyles-Ferris). Six 200 s frames covering the full error region were obtained in the  $g$  filter  $\sim 31.5$  hr after the X-ray trigger. These were promptly processed by the automatic pipeline and then by a modified version of the `photometry-sans-frustration` package<sup>44</sup> (M. Nicholl et al. 2023). The individual frames were aligned, stacked, and a template image from the Panoramic Survey Telescope and Rapid Response System (Pan-STARRS) subtracted using the ZOGY algorithm (B. Zackay et al. 2016) as implemented by the `PyZOGY` package (D. Guevel et al. 2021). A bright source was identified in the subtracted image and its flux measured from the stacked image using point-spread function



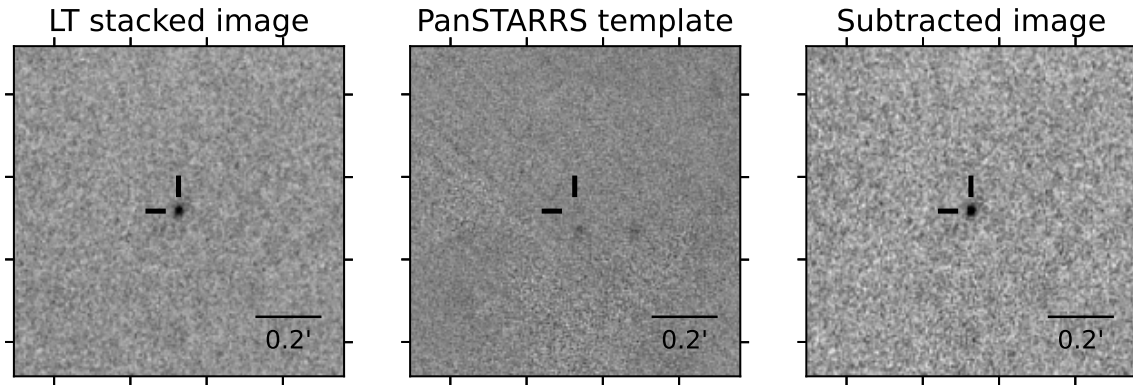
**Figure 1.** The UVOIR light curve of SN 2025kg’s fast cooling phase. The photometry has been corrected for Galactic extinction of  $A_V = 0.049$  (E. F. Schlafly & D. P. Finkbeiner 2011) using the K. D. Gordon et al. (2023) Milky Way model. The vertical lines indicate the times of our spectroscopic observations (with colors corresponding to Figure 4).

photometry calibrated to nearby Pan-STARRS stars. This source, later designated SN 2025kg, or the kangaroo, was promptly announced (R. A. J. Eyles-Ferris 2025). We show the discovery image in Figure 2. Additional optical photometry was obtained using LT/IO:O for two further nights during the fast cooling phase, covering the  $g$ ,  $r$ ,  $i$ , and  $z$  filters. These data were reduced using the same procedure as above.

We further obtained extensive photometric observations from the Nordic Optical Telescope (NOT) using the Alhambra Faint Object Spectrograph and Camera (ALFOSC) instrument (in *griz*; Program ID 70-301; PI: Jonker), the Sinistro imager on the Las Cumbres Observatory’s (LCO’s) South African Astronomical Observatory node 1 m telescope (*gr*; Program ID SUPA2024B-004; PI: Izzo), BlackGEM (*g*; P. J. Groot et al. 2024; Local Transient Survey program), and Gemini-South’s FLAMINGOS2 (*JH*; Program ID GS-2024B-Q-105; PI: Rastinejad). These data

<sup>44</sup> <https://github.com/mnicholl/photometry-sans-frustration>





**Figure 2.** The discovery image of SN 2025kg. The stacked LT IO:O  $g$ -band image is shown on the left, the Pan-STARRS template is shown in the center, and the subtraction is shown on the right. The images are oriented with north to the top and east to the left and the position of SN 2025kg is marked with the cross hairs.

were processed using their respective observatory’s pipelines and the flux of SN 2025kg was measured using standard methods. Acquisition images from our spectroscopic observations using the Very Large Telescope’s (VLT) X-shooter and Gemini-North’s GMOS-N were also analyzed to supplement our photometry.

To better characterize the properties of the source, particularly at higher energies than accessible through ground-based telescopes, we requested three Target of Opportunity (TOO) observations by the Neil Gehrels Swift Observatory (hereafter Swift). These were performed by Swift between 2025 January 10 and January 13. We acquired the resulting data from the UK Swift Science Data Centre<sup>45</sup> (UKSSDC) specifically those obtained by the X-ray Telescope (XRT) and Ultraviolet/Optical Telescope (UVOT). Given the blue nature of the transient, we requested observations in the  $u$ ,  $w1$ ,  $m2$ , and  $w2$  filters covering wavelengths from 3465 Å down to 1928 Å. We used UVOTPRODUCT V2.9<sup>46</sup> to measure SN 2025kg’s flux using a circular aperture with a radius of 5'' and a  $3\sigma$  detection threshold and converted to AB magnitudes using the standard UVOT zero-points (A. A. Breeveld et al. 2011).

To complete our photometry, we used the forced photometry services of the Asteroid Terrestrial-impact Last Alert System<sup>47</sup> (ATLAS; J. L. Tonry et al. 2018; K. W. Smith et al. 2020; L. Shingles et al. 2021) and the Zwicky Transient Facility (ZTF; F. J. Masci et al. 2019, 2023) to measure the flux at SN 2025kg’s position from a few days prior to its detection. For both observatories, we processed the forced photometry into single night epochs following the procedure detailed in the ZTF forced photometry documentation<sup>48</sup> with slight modifications for the ATLAS data. We set a  $5\sigma$  detection threshold and calculate  $3\sigma$  upper limits. In both cases, only upper limits were derived and we report these in Table 3 in Appendix A. Nevertheless, these upper limits are constraining, particularly a deep upper limit from ZTF  $\sim 2.3$  days prior to the trigger and an ATLAS upper limit only  $\sim 0.4$  days (observer frame) posttrigger.

We examine the evolution of the SED of the fast cooling phase by dividing the light curve into epochs and fitting them independently with a blackbody. We limit each epoch to covering up to 0.06 days (observer frame) and derive parameter distributions

using Monte Carlo analysis, varying the data within the errors and refitting 100 times. We plot the resulting SEDs in Figure 3 and present the inferred temperatures, radii, and luminosities in Table 1. We note that we have assumed the SED to be sufficiently accurately represented by a single blackbody. However, due to varying optical depth, ejecta temperatures, and other factors, the true SED is more likely a superposition of thermal and/or nonthermal emission. While we acknowledge these caveats (and in our advanced modeling below use a more complete description of the SED), this model provides a strong fit to the data and is useful for inferring the bulk properties of the transient and its evolution, guiding further analysis.

### 2.1.2. Spectroscopy

During the fast cooling phase of SN 2025kg, we obtained four spectra with the VLT, Gemini-North, and the Gran Telescopio Canarias (GTC). We summarize these observations and our data reduction here. Appendix A presents a log of our spectroscopic observations and we show the full spectral sequence in Figure 4.

Both VLT spectra were obtained with the X-shooter instrument (J. Vernet et al. 2011), a multiwavelength, medium-resolution spectrograph installed at the European Southern Observatory (ESO) VLT UT3/Melipal (Program ID 114.27PZ.001; PI: Tanvir). X-shooter covers a total range of  $\sim 3000$ – $25000$  Å with a slit width of 0.9 or 1.0 depending on the arm. Our VLT spectra were reduced using the standard ESOREFLEX pipeline (W. Freudling et al. 2013). Here, due to SN 2025kg’s blue nature and low redshift, we utilize only the data from the UV-Blue and Visible (VIS) arms covering  $\sim 3000$ – $10000$  Å, specifically the 1D spectra reduced in STARE mode. The arms were normalized to each other using their common wavelength area and each spectrum is flux calibrated using the closest photometry in time.

The Gemini-North spectrum was obtained with the GMOS-N instrument (Program ID GN-2024B-Q-107; PI: Rastinejad) with a slit width of 1''. The data were reduced using the PyEIT (J. Prochaska et al. 2020) package and again flux calibrated using photometry closest in time.

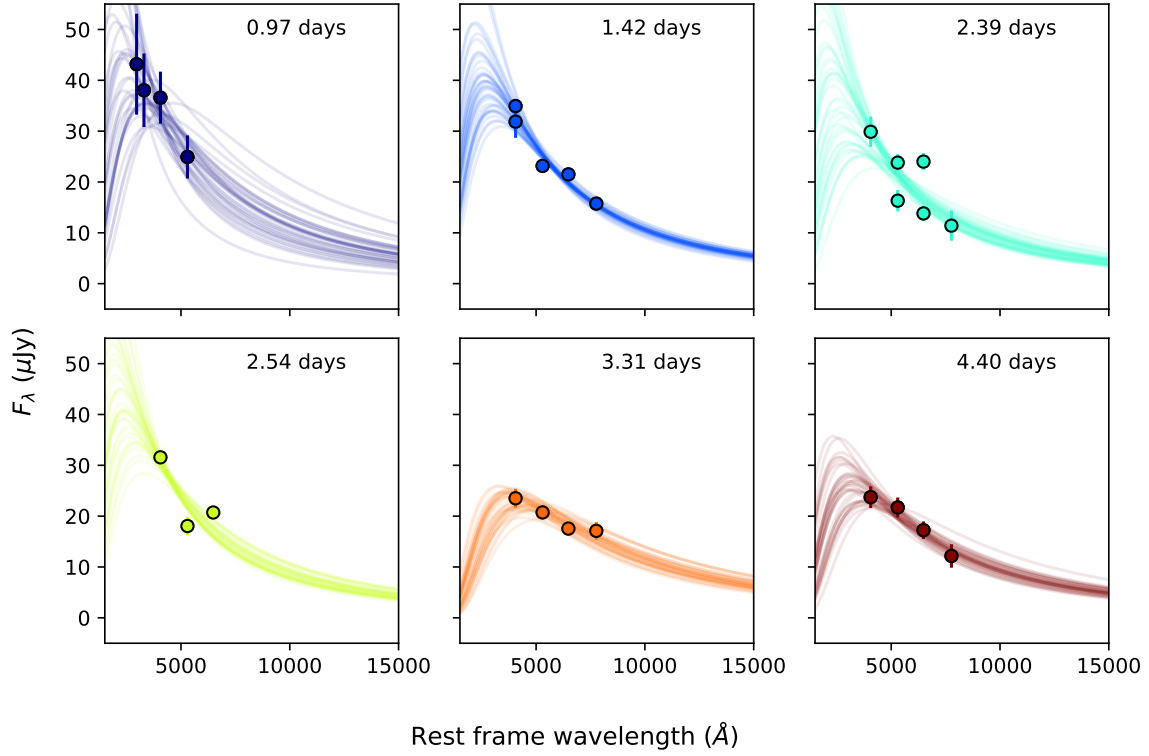
Finally, the OSIRIS+ instrument was used to obtain the spectrum observed by GTC (Program ID GTC1-24ITP; PI: Jonker). Data were obtained using both the R1000B and the R1000R gratings. A 1'' slit width was used for each of the two grating observations and the seeing as measured from the width of the spectroscopic trace is  $1.2 \pm 0.1$ '. We correct for

<sup>45</sup> <https://www.swift.ac.uk/index.php>

<sup>46</sup> As part of HEASOFT V6.32 (Nasa High Energy Astrophysics Science Archive Research Center ‘Heasarc’ 2014).

<sup>47</sup> <https://fallingstar-data.com/forcedphot/>

<sup>48</sup> [https://irsa.ipac.caltech.edu/data/ZTF/docs/ztf\\_forced\\_photometry.pdf](https://irsa.ipac.caltech.edu/data/ZTF/docs/ztf_forced_photometry.pdf)



**Figure 3.** The photometric SEDs of SN 2025kg at various epochs (given in the observer frame) fitted with sampled blackbody models.

**Table 1**

The Blackbody Properties Inferred from Fits to the Spectral Energy Distribution Derived from Various Epochs of Our Photometry

$\Delta t$ (days)	$T_{\text{bb}}$ ( $10^4$ K)	$R_{\text{bb}}$ ( $10^{15}$ cm)	$\log \left( \frac{L_{\text{bb,bol}}}{\text{erg s}^{-1}} \right)$
0.97150	$2.05^{+1.05}_{-0.55}$	$0.79^{+0.35}_{-0.25}$	$43.90^{+0.59}_{-0.22}$
1.42495	$1.91^{+0.30}_{-0.22}$	$0.83 \pm 0.10$	$43.83 \pm 0.14$
2.38689	$2.15^{+0.72}_{-0.48}$	$0.70 \pm 0.17$	$43.88 \pm 0.28$
2.54063	$2.21^{+0.58}_{-0.34}$	$0.69 \pm 0.13$	$43.91^{+0.22}_{-0.15}$
3.30612	$1.22^{+0.14}_{-0.10}$	$1.23 \pm 0.15$	$43.40 \pm 0.07$
4.37953	$1.57^{+0.32}_{-0.24}$	$0.91 \pm 0.17$	$43.55 \pm 0.14$

**Note.**  $\Delta t$  is given in the observer frame.

bias, flats, calibrate in wavelength using arc lamps, and optimally extract the spectra using PyRAF and MOLLY tasks. Subpixel drifts on the position of the [O I]  $\lambda 6300$  sky emission line were employed to correct for flexure effects on the wavelength calibration. The spectra were also corrected from the Earth movement using MOLLY tasks. Flux calibration was performed using observations of the flux standard G191-B2B at the end of the night. We corrected for slit losses, considering wavelength-dependent seeing as well as airmass correction. However, we note that the nonsimultaneous observation of the target and the standard introduces uncertainties to the flux calibration due to atmospheric variability.

To further constrain the properties of SN 2025kg, we fit our spectral continua with the same blackbody model previously applied to the photometric epochs. We use a signal-to-noise ratio (SNR) cut of  $\text{SNR} > 3$  per bin, fit only to those data and correct for Milky Way extinction using the same model and

$A_V = 0.049$  mag as our photometric analysis. In the case of the second X-shooter spectrum, due to the increasing opacity from elements formed by nucleosynthesis in the rising supernova, the spectrum is not purely thermal, particularly at blue wavelengths. We therefore apply an additional cut and fit only the data with an observed wavelength  $> 5500$  Å (4700 Å in the rest frame) with the blackbody. Blackbody spectra with parameters set to the median values (i.e., the values reported in Table 4 in Appendix A) are plotted in black over the spectrum for each epoch in Figure 4 and the inferred properties included in Table 4. Our results show that, consistent with the photometry, the spectral sequence is broadly consistent with a cooling, expanding blackbody.

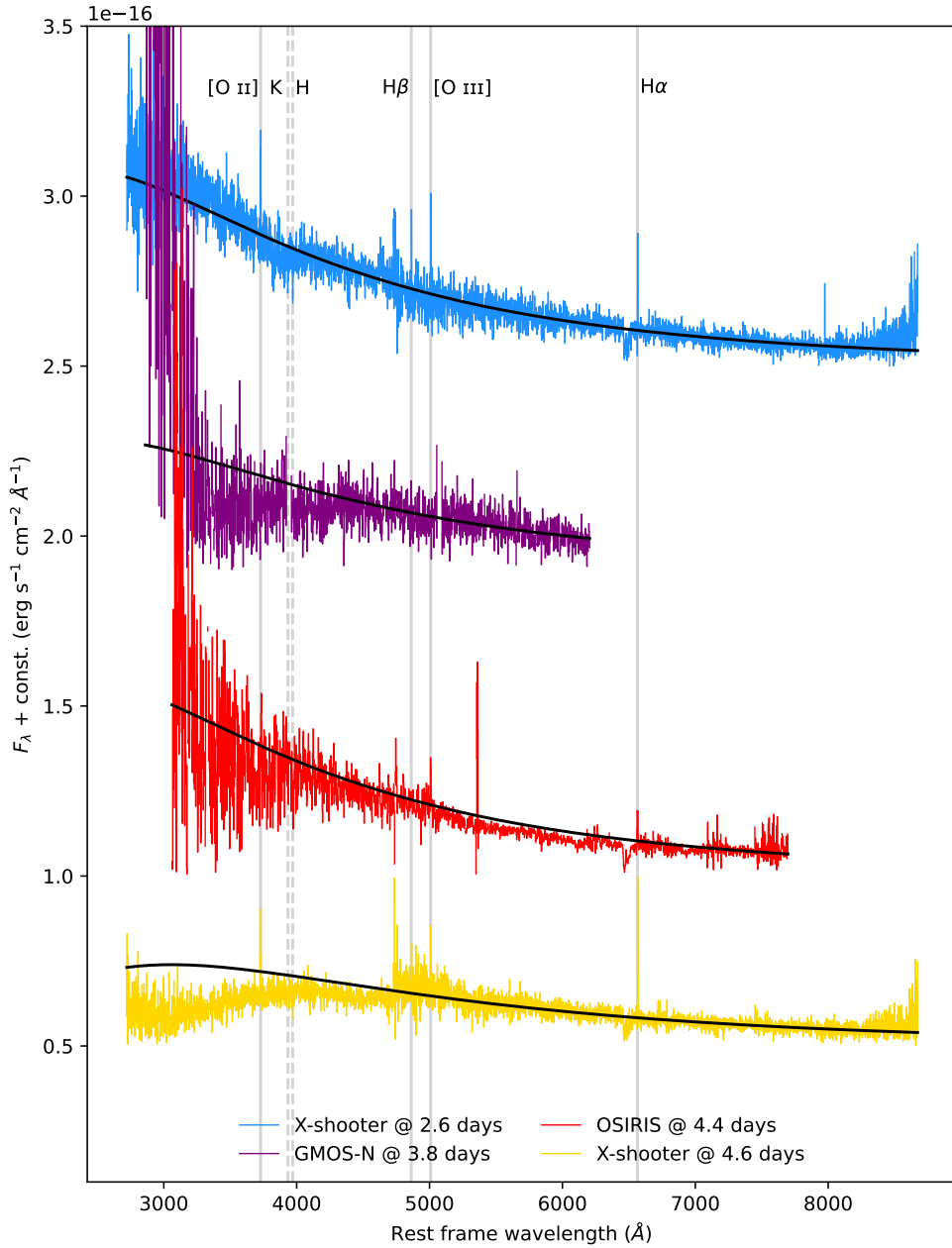
### 2.1.3. Redshift

Our spectroscopic observations reveal clear evidence for emission lines from the underlying host galaxy, including lines from [O II], [O III],  $H\beta$ , and  $H\alpha$  (see Figure 4). Measured from our first epoch X-shooter spectrum, these lines provide a systemic redshift for the host galaxy of  $z = 0.17641 \pm 0.0003$ . In addition we also observe absorption lines in the blue arm from Ca H and K at a similar consistent redshift of  $z = 0.17637 \pm 0.0002$ . In our cosmology, the luminosity distance is therefore 880.6 Mpc.

### 2.2. X-Rays

EP250108a was originally discovered in X-rays and we also performed additional observations to constrain its behavior at these energies. We summarize our observations and results in Appendix A and show the X-ray light curve of EP250108a in Figure 5, including the initial detection (R. Z. Li et al. 2025a, 2025c) and upper limit reported by R. Z. Li et al. (2025b).

We observed the field of EP250108a using XMM-Newton starting at 17:24:49 (UTC) on 2025 January 14 (Program ID 096168; PI: Jonker). The data were processed with SAS



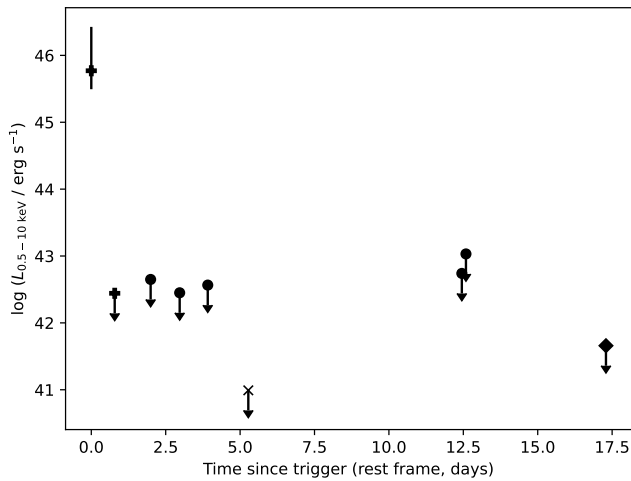
**Figure 4.** The spectral sequence of SN 2025kg’s fast cooling phase with times given in the observer frame. Emission and absorption lines typically detected in galaxy spectra are marked in solid and dashed gray lines, respectively. In addition, blackbody fits to each continuum (see text) are plotted in black.

version 20230412\_1735. After filtering for background flares the effective exposure for the pn detector is 30.44 ks, while it is 48 and 47.4 ks for the MOS1 and MOS2 detectors, respectively. However, for the MOS1 and MOS2 detectors we could only choose a source-free background region on an adjacent detector as the use of the prime partial window of the central detector limited the field of view covered by that detector, leaving no room to estimate the background effectively. Given the larger uncertainties associated with estimating the background on another detector, and because of the higher PN sensitivity, we only consider the PN detector measurements for our upper limit calculations. From visual inspection of the image made from the filtered PN data we conclude we do not detect a source at the position of the optical transient. We calculated the number of source counts needed to be detected in a circle of  $10''$  radius in order to be  $3\sigma$  above the expected background in such a region in

the energy range 0.5–10 keV. We used this number of 64 counts to calculate a 95% confidence upper limit on the 0.5–10 keV unabsorbed source flux of  $\lesssim 1 \times 10^{-15} \text{ erg cm}^{-2} \text{ s}^{-1}$  assuming a power-law spectrum with index = 3.03 as observed by R. Z. Li et al. (2025c).

We obtained further observations with the Chandra X-ray Observatory (Director’s Discretionary Time Program ID 30747; PI: Jonker). An observation was obtained starting at 20:35:15 (UTC) on 2025 January 28 for 10.851 ks. The source was placed at the default location on the ACIS-S3 chip, which was operated in the VERY FAINT mode.

The Chandra data were processed using CIAO v4.16. We detect no photons in a circle of  $1''$  radius centered on the source localization. Using the method of R. P. Kraft et al. (1991) we obtain a 90% confidence upper limit of 2.3 counts. Again assuming the spectrum observed by R. Z. Li et al. (2025c), this



**Figure 5.** The X-ray light curve of EP250108a including data available in GCNs from EP (R. Z. Li et al. 2025b, 2025c, pluses) and from our observations with XMM-Newton (cross), Chandra (diamond), and Swift (circles). Note the EP detection is the luminosity from 0.5 to 4 keV as given in R. Z. Li et al. (2025c).

corresponds to a 0.5–10 keV unabsorbed source flux upper limit of  $5 \times 10^{-15} \text{ erg s}^{-1} \text{ cm}^{-2}$ .

We also investigate the X-ray data acquired by Swift in our TOO observations, plus two additional observations also undertaken by Swift. No source was identified in any single observation. The Living Swift-XRT Point Source Catalog Upper Limit Server<sup>49</sup> (P. A. Evans et al. 2023) automatically derives  $3\sigma$  upper limits, which range from 0.002 to 0.009 counts  $\text{s}^{-1}$ . Using PIMMS V4.15 and the spectrum reported in R. Z. Li et al. (2025c), this indicates unabsorbed 0.5–10 keV flux upper limits of  $3.1 \times 10^{-14}$ – $1.2 \times 10^{-13} \text{ erg cm}^{-2} \text{ s}^{-1}$ . Along with the XMM-Newton and Chandra data, we convert these to luminosities and include them in Table 5 in Appendix A.

### 2.3. Radio

We observed the position of EP250108a with the MeerKAT radio telescope (F. Camilo et al. 2018; J. Jonas 2018), as part of program SCI-20241101-FC-01 (PI: F. Carotenuto). Our observing log is given in Appendix A. We conducted four observations log spaced in time, each with the same total on-source time of 42 minutes. The first observation started on 2025 January 13 at 17:57 UTC (5.2 days after the first X-ray detection). The second and third observations were performed on 2025 January 30 at 13:41 UTC (22.0 days after the first X-ray detection) and 2025 February 20 at 15:55 UTC (43.2 days after the first X-ray detection), respectively. A fourth observation was performed on 2025 April 3 at 09:24 UTC (84.9 days after the first X-ray detection).

We observed at a central frequency of 3.06 GHz (S band, S4), with a total bandwidth of 875 MHz. PKS J1939–6342 and PKS J0409–1757 were used as flux and complex gain calibrators, respectively. The data were reduced with the OXKAT pipeline (I. Heywood 2020), which performs standard flagging, calibration, and imaging using *tricolour* (B. V. Hugo et al. 2022), CASA (Team CASA et al. 2022), and WSCLEAN (A. R. Offringa et al. 2014), respectively. In the imaging step, we adopted a Briggs weighting scheme with a  $-0.3$  robust

parameter, yielding a  $2.8 \times 2.8$  beam and a  $8 \mu\text{Jy beam}^{-1}$  rms noise in the target field.

We do not detect radio emission at the position of the optical counterpart of EP250108a, and we place a  $3\sigma$  upper limit on the flux density of the target at 24, 24, 27, and 26  $\mu\text{Jy beam}^{-1}$  for the first, second, third, and fourth observation, respectively.

### 3. SN 2025kg and Other Transients with Early Thermal Features

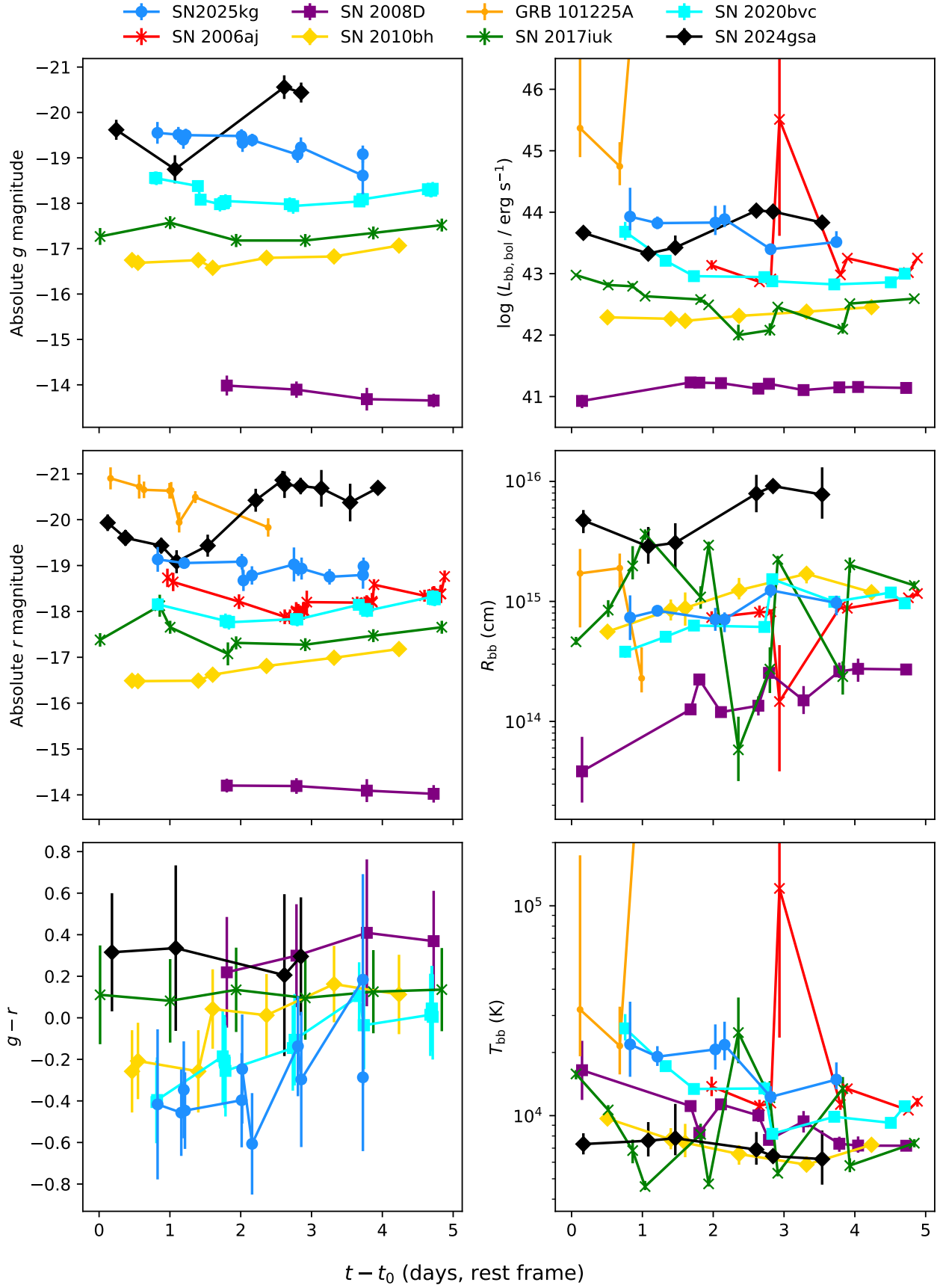
EP’s unprecedented observational capabilities are likely to uncover a significant population of events similar to EP250108a/SN 2025kg in the near future. For instance, a source with similar optical properties, EP250304a (W. Chen et al. 2025; X. Liu et al. 2025a; K. L. Page et al. 2025; A. Saccardi et al. 2025; S. P. R. Shilling & Swift UVOT Team 2025), was detected during the preparation of this letter. However, there are also a number of previously detected core-collapse supernovae with similar cooling phases. Here we compare the observed properties of SN 2025kg to a selection of these supernovae including SN 2006aj (S. Campana et al. 2006; P. Ferrero et al. 2006; N. Mirabal et al. 2006; J. Sollerman et al. 2006), SN 2008D (P. A. Mazzali et al. 2008; A. M. Soderberg et al. 2008; D. Malesani et al. 2009; M. Modjaz et al. 2009), SN 2010bh (Z. Cano et al. 2011; F. Bufano et al. 2012; E. F. Olivares et al. 2012), SN 2017iuk (V. D’Elia et al. 2018; L. Izzo et al. 2019), SN 2020bvc (A. Y. Q. Ho et al. 2020a; L. Izzo et al. 2020; J. Rho et al. 2021), and SN 2024gsa (H. Sun et al. 2025; S. Srivastav et al. 2025; J. N. D. van Dalen et al. 2025). Of these, SN 2024gsa is particularly notable as the optical counterpart to EP240414a, an FXT also detected by EP. There are also several supernovae that show rapid rises, possibly due to early contributions from shock heating or cocoon emission, such as iPTF16asu (L. Whitesides et al. 2017; L. J. Wang et al. 2019) and SN 2018gep (A. Y. Q. Ho et al. 2019). However, these sources lack a distinct early phase common to the rest of our sample and we therefore do not compare directly here. All of the above sources are Ic-BL supernovae (i.e., the same type as SN 2025kg) with the exception of SN 2008D, which is a Type Ib (D. Malesani et al. 2009) and therefore likely has a progenitor with a more intact helium envelope. We also compare to GRB 101225A (S. Campana et al. 2011; C. C. Thöne et al. 2011; A. J. Levan et al. 2014), an ultralong GRB with an early blue component before becoming more consistent with a typical GRB afterglow. In J. C. Rastinejad et al. (2025), we extend the comparison to the properties of the supernovae themselves i.e., at later times than examined here. In Appendix C, we also compare SN 2025kg’s early behaviour to the LFBOT sample, although we find significant differences in those cases.

In Figure 6, we plot the absolute magnitude and color evolution of these supernovae. In addition, we also fit blackbodies to individual epochs of these supernovae’s early components using the same procedure as detailed in Section 2.1 allowing us to directly compare the temperature, radius, and luminosity evolution.

We find that SN 2025kg most closely resembles SN 2006aj and SN 2020bvc. Its blackbody radius, in particular, is in very strong agreement with the early phases of these supernovae although SN 2025kg is somewhat hotter and therefore of higher luminosity. There is greater discrepancy with SN 2008D, SN 2010bh, GRB 101225A, SN 2017iuk, and SN 2024gsa, although there is difficulty in comparing the latter as there are likely to be overlapping emission components during the early

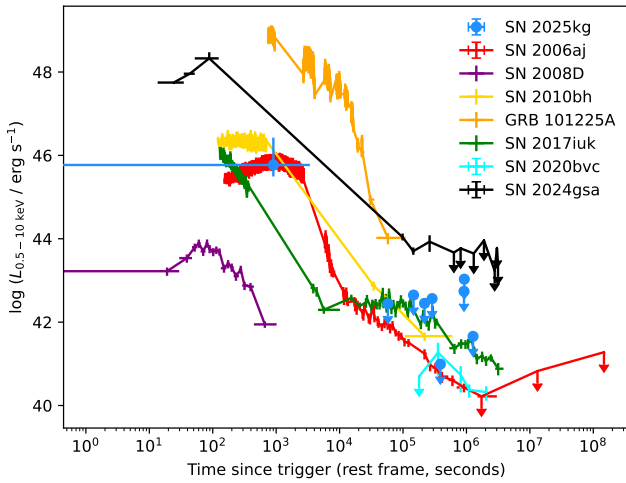
<sup>49</sup> <https://www.swift.ac.uk/LSXPS/ulserv.php>





**Figure 6.** The photometric and blackbody properties of SN 2025kg's fast cooling phase compared to the properties of supernovae with similar early features. We include GRB 101225A, which also displays a resemblant feature. In the case of SN 2006aj, we have used the Bessell  $R$  filter as a proxy for the  $r$  filter.





**Figure 7.** The X-ray light curve of EP250108a compared to our sample of FXT-GRB supernovae. EP250108a is shown in blue.

phase (H. Hamidani et al. 2025b; S. Srivastav et al. 2025; J. N. D. van Dalen et al. 2025; J.-H. Zheng et al. 2025). Even accounting for this, however, SN 2024gsa appears to show more rapid radius and luminosity evolution than SN 2025kg but it and both SN 2010bh and SN 2017iuk are somewhat cooler. GRB 101225A’s early optical counterpart is much more luminous but its temperature and radius evolution are somewhat poorly constrained by our methods here. The more in depth modeling of C. C. Thöne et al. (2011) indicates a significantly higher temperature but smaller radius, pointing toward a different origin than SN 2025kg’s early fast cooling phase.

Finally, while SN 2008D does show a similar slope in its temperature evolution (notably A. M. Soderberg et al. 2008 show  $T \propto t^{-0.5}$  consistent with our result in Section 4.2), it is much cooler, less luminous, and has a smaller radius. This is consistent with a separate origin for the early phase of SN 2008D as a shock breakout from the helium envelope of a Type Ib progenitor (e.g., A. M. Soderberg et al. 2008) rather than a cocoon or CSM interaction as suggested by our analyses in this work.

In Figure 7, we compare the X-ray light curves of our sample to EP250108a/SN 2025kg, taken either from the references above or acquired from the UKSSDC. Again we find a strong agreement with SN 2006aj and SN 2020bvc—in particular SN 2006aj’s light curve is entirely consistent with the observed data and limits from EP250108a. We also find a strong agreement with SN 2010bh/XRF 100316D and while SN 2017iuk/GRB 171205A’s light curve is not particularly well constrained at early times and hints toward a significantly higher luminosity, it is also broadly compatible. As expected, GRB 101225A and SN 2024gsa are significantly more luminous suggesting either a different origin, e.g., afterglow emission or continued central engine activity in GRB 101225A. Another possibility, which we explore in depth in Section 4, is that while all the X-ray emission in the above cases is powered by some kind of relativistic jet, SN 2006aj’s, SN 2020bvc’s, and SN 2025kg’s jet is either significantly less powerful or is unable to break out of its progenitor’s outer envelope or the surrounding CSM. Such a jet is deemed to be “failed” (e.g., E. Nakar 2015; E. Nakar & T. Piran 2017; A. L. Piro & J. A. Kollmeier 2018; H. Hamidani et al. 2025a) and the resulting high-energy emission is much fainter. The material accelerated by the jet may instead form a rapidly expanding cocoon, which produces

the bulk of the observed emission. SN 2008D is again much fainter as expected from its obviously different origin.

At radio wavelengths and including the limits from G. Schroeder et al. (2025) and T. An et al. (2025), we find SN 2025kg is again compatible with SN 2020bvc (A. Y. Q. Ho et al. 2020a) and SN 2006aj’s radio counterparts (A. M. Soderberg et al. 2006). This is consistent with a picture where all of these events either had similar weak or failed jets or, as suggested elsewhere (e.g., B. E. Cobb et al. 2006; K. Toma et al. 2007; S. W. K. Emery et al. 2019), were observed at least somewhat off axis. In contrast, SN 2017iuk and SN 2024gsa are significantly brighter in the radio than SN 2025kg, again suggesting that if they had emerged from a similar progenitor system, a powerful jet successfully broke out. We are unable to compare to SN 2010bh due to a lack of data.

To summarize, we find SN 2025kg to be similar to SN 2006aj and SN 2020bvc suggesting both that similar progenitors powered all these events and that the environments surrounding the explosion were similar. In particular, it is likely that if there were jets, they were either relatively low energy and/or failed to break out. There are also some similarities to SN 2017iuk and SN 2024gsa but these particular events were more likely to have successful jets. In particular, SN 2024gsa is significantly more luminous at both X-ray and radio energies. SN 2017iuk, on the other hand, is roughly compatible in X-rays with SN 2025kg but its radio is much brighter, suggesting this could be a case of a somewhat off-axis but successful jet. The resemblance between SN 2010bh and SN 2017iuk also suggests a similar nature for the former. The additional optical component in SN 2024gsa may arise due to the presence of both a cocoon and dense CSM emission (J. N. D. van Dalen et al. 2025) or could be the result of a more successful jet (H. Hamidani et al. 2025b; J.-H. Zheng et al. 2025). On the other hand, both GRB 101225A and SN 2008D show significant differences to SN 2025kg, however, and are likely to be the result of substantially different systems.

As explored in J. C. Rastinejad et al. (2025), the supernovae themselves in SN 2006aj, SN 2020bvc, SN 2024gsa, and SN 2025kg also show distinct similarities that further tie these events together and suggest similar origins.

## 4. The Nature of EP250108a/SN 2025kg

### 4.1. Energetics

To explore the origins of EP250108a/SN 2025kg, we first evaluate the observed energetics. At the luminosity distance of EP250108a, the flux reported by R. Z. Li et al. (2025c) equates to a luminosity of  $5.9^{+20.9}_{-2.8} \times 10^{45} \text{ erg s}^{-1}$  and the 2200 s assumed duration of the FXT implies a total isotropic-equivalent energy of  $1.3^{+4.6}_{-0.6} \times 10^{49} \text{ erg}$  in the 0.5–4 keV band. M. E. Ravasio et al. (2025) also place constraints on higher-energy emission using the Gamma-ray Burst Monitor instrument on the Fermi satellite. In the 10–1000 keV band, any emission is limited to an isotropic-equivalent luminosity  $\lesssim 2.4 \times 10^{48} \text{ erg s}^{-1}$ .

The energy is therefore  $\sim 2$  orders of magnitude lower than the bulk of the long-GRB population (e.g., L. Nava et al. 2012). If we implicitly assume that the jet did break out but did not produce gamma rays in our observable window (M. E. Ravasio et al. 2025), we can constrain the luminosity of such a jet. Only bursts with peak isotropic-equivalent gamma-ray luminosities under  $\sim 10^{49} \text{ erg s}^{-1}$  are viable,

**Table 2**

The Priors and Inferred Values from Our Fit to SN 2025kg’s Fast Cooling Phase Light Curve with Our Cooling, Expanding Blackbody Model

Parameter	Prior	Fitted Value
$R_0$	$>1 \times 10^{12}$ cm	$5.81^{+1.46}_{-1.06} \times 10^{14}$ cm
$v_0$	$0.0 < v_0 < c$	$5.00^{+2.58}_{-1.81} \times 10^9$ cm s $^{-1}$
$\tau_d$	$>0.0$ s	$1.32^{+3.44}_{-0.87} \times 10^6$ s
$\alpha_d$	$0.0 < \beta < 10.0$	$6.10^{+2.85}_{-3.28}$
$T_0$	$>0.0$ K	$2.92^{+1.25}_{-0.59} \times 10^4$ K
$\tau_c$	$>0.0$ s	$3.79^{+6.21}_{-2.46} \times 10^4$ s
$\alpha_c$	$0.0 < \alpha < 1.0$	$0.49^{+0.21}_{-0.13}$
$f$	$-10.0 < \log f < 1.0$	$-2.00^{+0.18}_{-0.19}$

leaving only low-luminosity GRBs (e.g., E. Liang et al. 2007; F. J. Virgili et al. 2009). These GRBs have significantly lower luminosities than the majority of the population and often have softer prompt emission (M. Patel et al. 2023). The reasons for the stark differences between these sources and other GRBs are not entirely clear but one possibility is intrinsically weaker or possibly failed jets (e.g., E. Nakar 2015; N. Senno et al. 2016) as suggested by our comparison to similar transients.

#### 4.2. Photometric Modeling

To fully explore the evolution of SN 2025kg’s fast cooling phase, we first fit the full light curve using a simple cooling, expanding blackbody model. While this is primarily a phenomenological model, we can infer the apparent temperature and luminosity evolution. Assuming the photospheric radius broadly coincides with the expanding shock or cocoon and that the resulting emission is thermally dominated,<sup>50</sup> this model also provides some initial constraints on the expansion velocity. As noted above, we are simplifying the presumably complex superposition of various emission components that make up the true SED. However, this procedure is useful for the constraints that can be fed into our other modeling.

We assume the photospheric radius varies as

$$R_{\text{ph}}(t) = R_0 + \int_{t_0}^t v(t) dt, \quad (1)$$

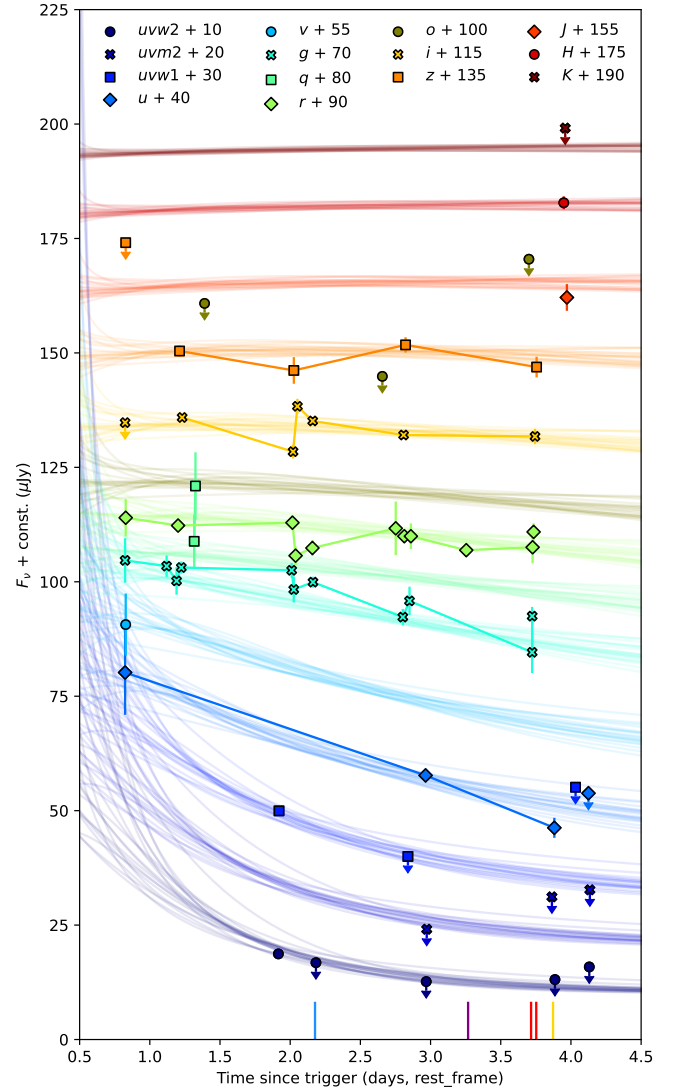
where  $R_0$  is the radius of the photosphere at  $t_0 = 0.5$  days (rest frame) after the EP/WXT trigger time, and  $v(t)$  is the expansion velocity:

$$v(t) = v_0 \left( \frac{t + \tau_d}{\tau_d} \right)^{-\alpha_d}, \quad (2)$$

where  $v_0$  is the expansion velocity at  $t_0 = 0.5$  days (rest frame) after the trigger time,  $\tau_d$  is the deceleration timescale, and  $\alpha_d$  is positive. Similarly, the temperature evolution is assumed to vary as

$$T(t) = T_0 \left( \frac{t + \tau_c}{\tau_c} \right)^{-\alpha_c}, \quad (3)$$

where  $T_0$  is the temperature at  $t_0 = 0.5$  rest-frame days after the EP/WXT trigger time,  $\tau_c$  is the cooling timescale, and  $\alpha_c$  is positive. We do not include any additional extinction component intrinsic to the host. However, if we do fit for such a component



**Figure 8.** The UVOIR light curve of SN 2025kg’s fast cooling phase fitted with our cooling, expanding blackbody model. We show traces from 20 randomly selected fits in our MCMC chain. The vertical lines indicate the times of our spectroscopic observations (with colors corresponding to Figure 4).

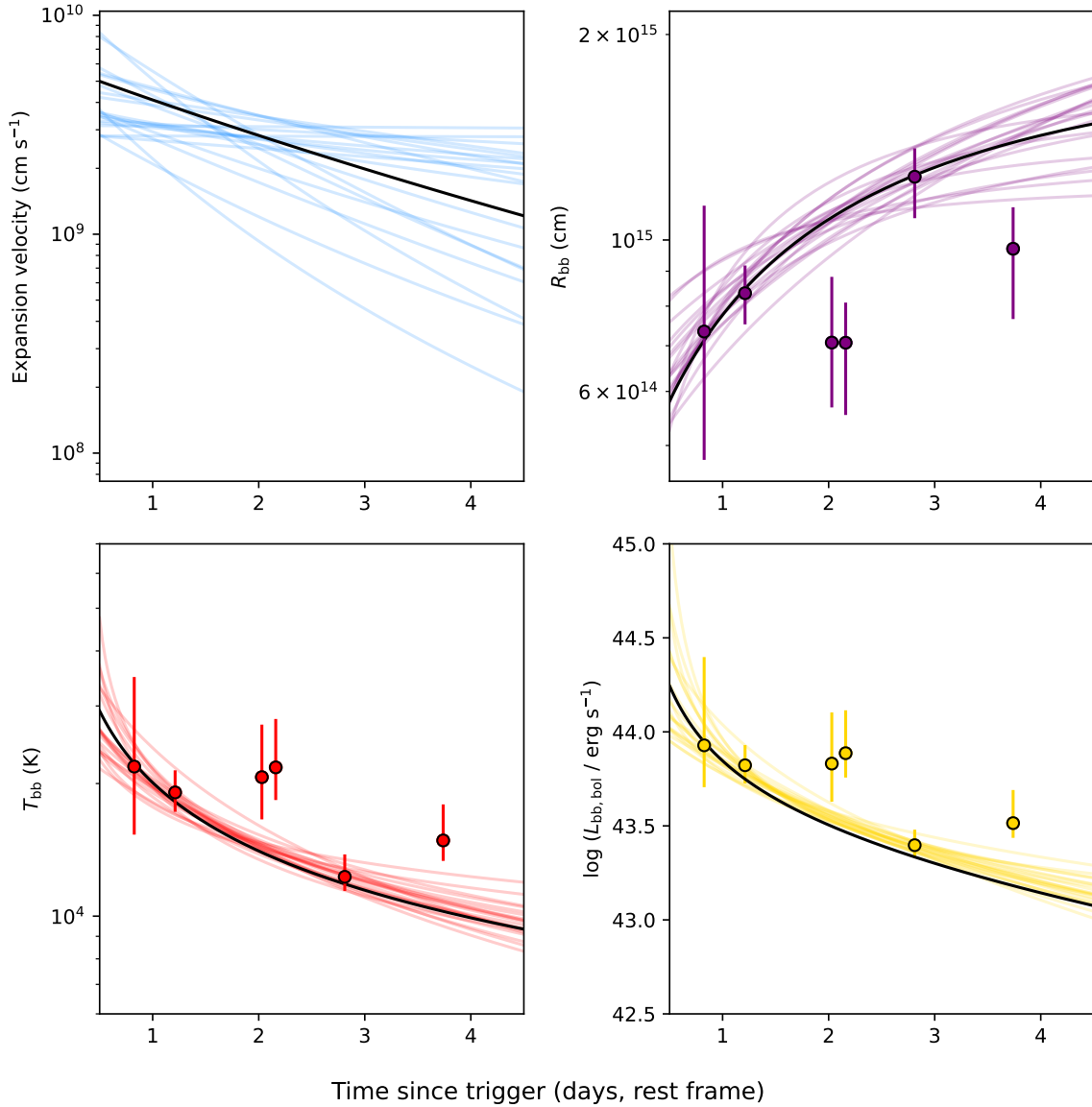
using `dust_extinction` and the K. D. Gordon et al. (2024) averaged model for the Small Magellanic Cloud, we find  $A_{V,\text{host}} \sim 0.2$  mag and our other results to be broadly consistent within the errors.

We fit this model to SN 2025kg’s light curve using the Markov Chain Monte Carlo (MCMC) algorithm implemented in `emcee v3.1.6` (D. Foreman-Mackey et al. 2013) with 32 walkers. We use 5000 iterations, discarding the first 500 as burn in, and include an additional parameter  $f$  representing the fractional underestimation of our errors.<sup>51</sup> We summarize our priors in Table 2.

As shown in Figure 8, we find this model is a reasonable representation of the light curve in the fast cooling phase. We give our inferred parameters in Table 2 and show a corner plot in Appendix B. The inferred temperature, radius, and bolometric luminosity evolution of the fast cooling phase are

<sup>50</sup> Or is at least quasi thermal.

<sup>51</sup>  $f$  enters into our likelihood function as an additional factor of  $F_{\nu, \text{model}} e^{\log f}$  added in quadrature to the measured errors.



**Figure 9.** The velocity, radius, temperature, and luminosity evolution of SN 2025kg’s fast cooling phase inferred from our cooling, expanding blackbody model with traces from the same fits as in Figure 8. The black lines in each panel indicate the evolution derived when using the median of each parameter (i.e., the values reported in Table 2). We also plot the properties inferred from our blackbody fits to our photometric epochs (circles) and spectroscopic continua (crosses).

shown in Figure 9 and are in good agreement with the values inferred from blackbody fits to the photometric epochs and our spectroscopic observations (see above). We note that the model slightly underpredicts the  $g$  band and overpredicts the UV bands ( $u$ ,  $uvw1$ ,  $uvm2$ , and  $uvw2$ ). This is likely due to us neglecting the effect of increasing opacity as heavy elements are formed in the rising supernova, an effect modeled in detail below, and possibly due to underestimating the deceleration of the photosphere at late times (see top right panel of Figure 9).

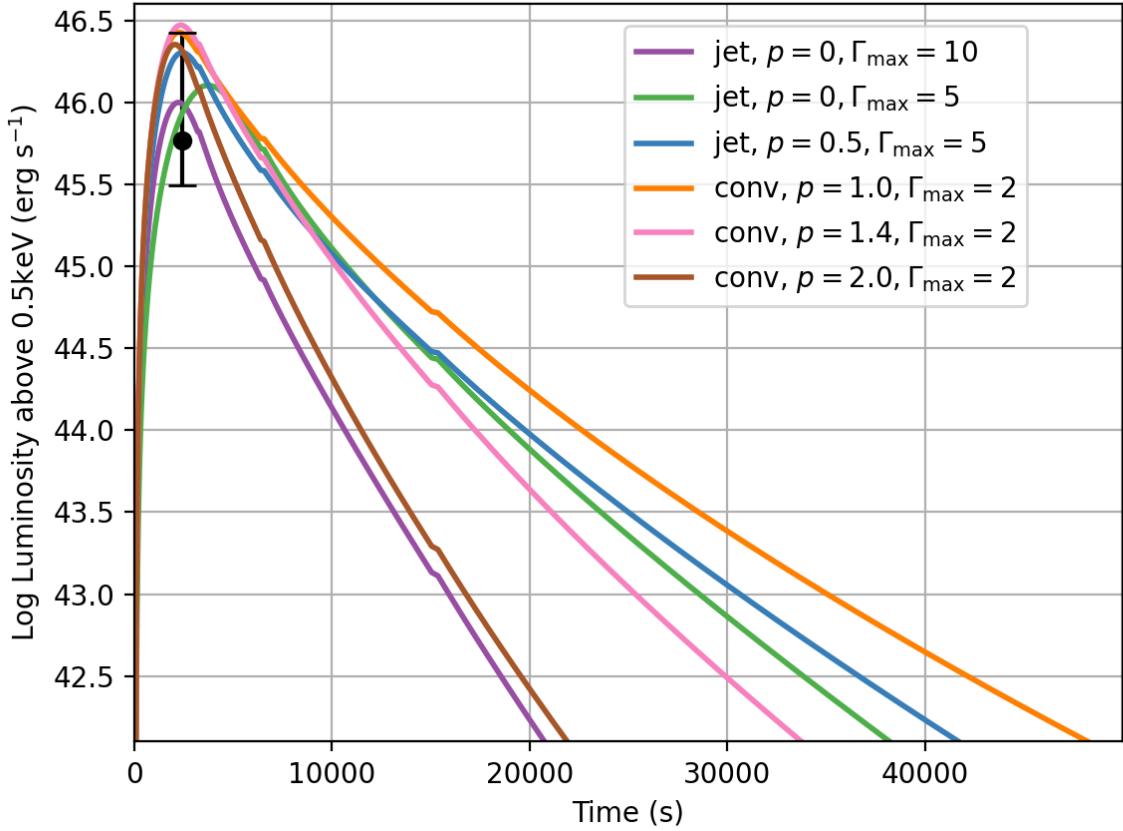
Our results also indicate that the initial expansion velocity of SN 2025kg was at least mildly relativistic—the inferred  $R_0$  would require an average expansion velocity over the first 0.5 rest-frame days of  $\sim 1.3 \times 10^{10} \text{ cm s}^{-1}$  or  $\sim 0.45c$ . However, this is inconsistent with a simple extrapolation of the inferred velocity evolution. This suggests the early expansion velocity is much faster before rapidly decelerating to match the value inferred at 0.5 days. To constrain this further, we repeat our fit with  $v_0$ ,  $R_0$ , and  $T_0$  as the expansion velocity, radius, and temperature at the trigger time. We fix  $R_0 = 10^{12} \text{ cm}$ , i.e., the

largest radius expected for the presumed Wolf–Rayet progenitor and find  $v_0 \sim 0.6c$ . This is maintained for  $\sim 8 \text{ hr}$  before a rapid deceleration. We note, however, that this fit is an extrapolation of later data and the velocity and temperature evolution are significantly more complex than we have assumed.

We can however compare the EP/WXT data with the prediction from this model of a soft, thermal X-ray source at the trigger time. Such a source is inconsistent with the harder observed spectrum of the transient (R. Z. Li et al. 2025c; W. X. Li et al. 2025), indicating a different origin for the X-ray and early optical emission. We explore this further in Sections 4.3 and 4.5.

#### 4.3. Origin of the X-Ray Emission

Having established that the same thermal transient is unlikely to generate both the X-ray and optical emission, we now investigate the source of the FXT itself. The luminous



**Figure 10.** X-ray luminosities as a function of time from the high-velocity ejecta. Here we assume two basic models: a convective engine where the high-velocity ejecta are produced as the shock propagates out of the stellar edge, and a jet-driven model where the high-velocity ejecta are dictated by the failed jet + cocoon ejecta. These models are differentiated by the distribution (mass as a function of ejecta velocity) and the maximum Lorentz factor of the ejecta.

X-ray signal can be explained through Bremsstrahlung emission arising from a large mass of material moving at a high velocity. From the massive star progenitor of EP250108a, this could be from either shock heating in the supernova blastwave or the propagation of a failed jet through the star or clumpy stellar wind. Here, we use the framework developed in C. L. Fryer et al. (2025, in preparation) to explore these possibilities.

The fastest ejecta are described by a distribution of velocities and the combined emission from this distribution produces the observed X-rays. For the energy distribution of high-velocity ejecta, we use a simple power law:

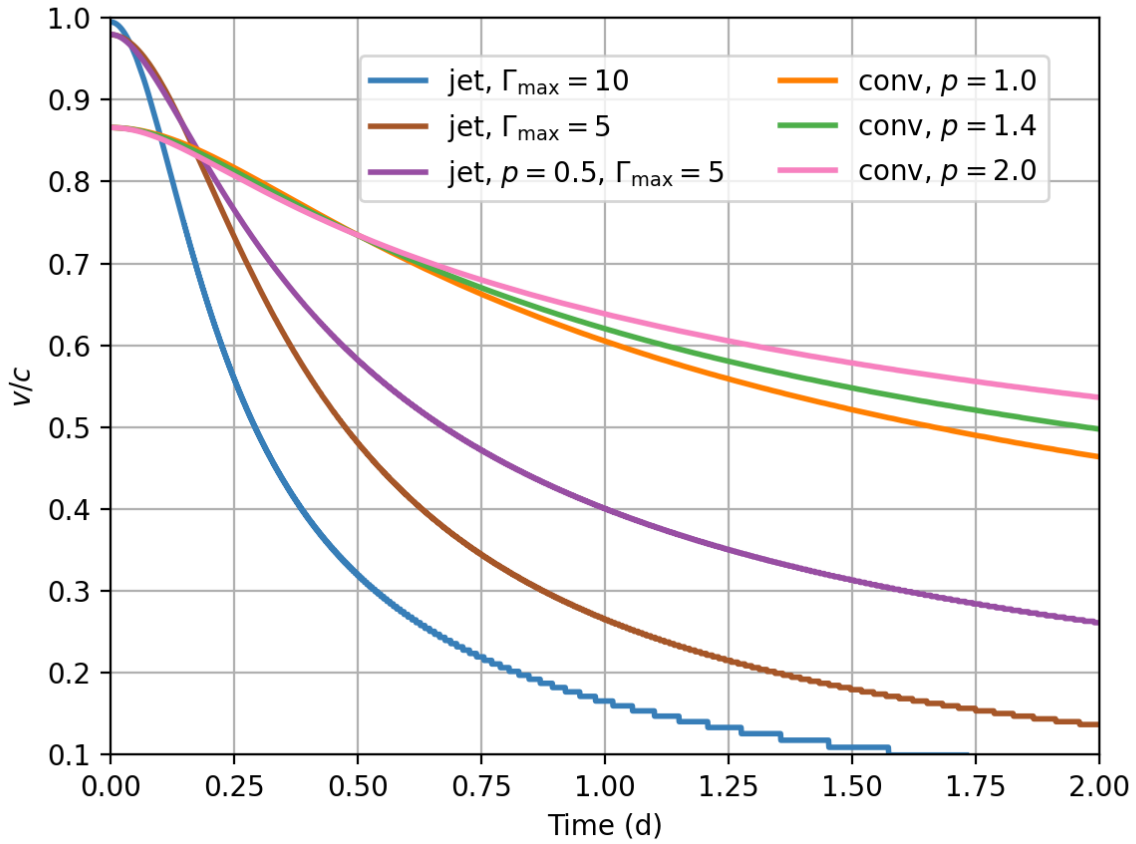
$$E(\Gamma\beta) \propto (\Gamma\beta)^{-p} \quad \text{for } \Gamma < \Gamma_{\max} \\ = 0 \text{ otherwise,} \quad (4)$$

where  $\Gamma$  is the Lorentz factor,  $\beta$  is the velocity divided by the speed of light, and  $p$  describes the velocity distribution. We explore two different engine scenarios known to power massive star explosions. The first is a convective engine where the core collapse results in a hot protoneutron star (e.g., S. E. Woosley 1993; M. Herant et al. 1994) and is expected in the vast majority of core-collapse supernovae. The neutrino luminosity of the remnant drives a blastwave which generates a relativistic component ( $\Gamma_{\max} \sim 2$ ) from shock acceleration as it exits the star. The second is a collapsar engine where the star explodes through a combination of disk winds and collimated jets. This engine was invoked to explain long GRBs and their associated Ic-BL supernovae (A. I. MacFadyen & S. E. Woosley 1999;

S. E. Woosley & J. S. Bloom 2006) and may also explain other Ic-BL supernovae (C. L. Fryer et al. 2025). In this case, the jet fails to efficiently break out of the star’s outer envelope or CSM and the resulting ejecta are a semirelativistic cocoon ( $\Gamma_{\max} \sim 5 - 10$ ) of a baryon-loaded jet ejecta. For this failed jet model, we assume the velocity distribution is relatively flat ( $p = 0-0.5$ ). For the convective engine, we use steeper slopes ( $p \sim 2-4$ ) to match shock acceleration as the blastwave breaks out of the star (J. C. Tan et al. 2001).

We find that we can reproduce the peak luminosity, half-peak duration, and the rapid decay with both convective and jet-driven models under certain parameters. We show several such models in Figure 10 and can use the parameters inferred from this modeling to place lower limits on the mass moving at high velocities. For our jet-driven model, matching the observed X-ray data requires roughly  $10^{-4}-10^{-3} M_{\odot}$  of ejecta with velocities above  $0.1c$ . This is consistent with recent calculations of the breakout of the jet-driven cocoon (E. M. Gutiérrez et al. 2025). For our convective-engine model with a shallow power law ( $p = 2$ ), we are able to fit the data only if we assume the high-velocity ejecta ( $\beta > 0.1$ ) exceed  $1 M_{\odot}$ . We can reduce this requirement by more than an order of magnitude (down to  $0.04 M_{\odot}$ ) by flattening the velocity distribution ( $p \sim 1$ ). For the convective engine, the energy is limited to 2 to 3 times the energy at the launch of the explosion. For current supernova progenitor models, the total explosion energy is limited to  $\sim 1-3 \times 10^{51}$  erg (C. L. Fryer & V. Kalogera 2001). Although long-lived engines can increase the total energy by a factor of  $\sim 2$ , most convective-driven





**Figure 11.** Model photospheric velocity of the shock breakout/interaction models from Figure 10. The high mass in the convective-engine models causes them to decelerate slowly, arguing for a high-velocity photosphere in the first 2 days. The lower mass in the jet-driven explosions leads to rapid deceleration of the photosphere.

engine simulations have comparable energies to the explosion energy. These models are expected to have less than  $0.001\text{--}0.01 M_{\odot}$  of ejecta at the required high ( $\beta > 0.1$ ) velocities (C. L. Fryer et al. 2018). We can therefore only produce X-ray signals that match the observations in an extreme case where we both assume supernova energies exceeding current models and push the limits of the mass/energy distribution with ejecta velocity.

We can further constrain the shock interaction conditions by following the evolution of our fast-moving ejecta in the first few days and, in particular, the velocity of the photosphere. The progenitors of Type Ic supernovae can eject material from their outer envelope as they approach core collapse in the form of stellar winds (e.g., L. Dessart et al. 2020). As the ejecta propagate through this stellar wind, they will sweep up mass and decelerate. At the same time, as they become optically thin, the photosphere recedes relative to the outflowing ejecta, thus probing slower-moving inner material. To calculate the photospheric velocity, we assume the mass of the CSM is set by a wind profile, and the enclosed mass out to radial extent  $R$  is

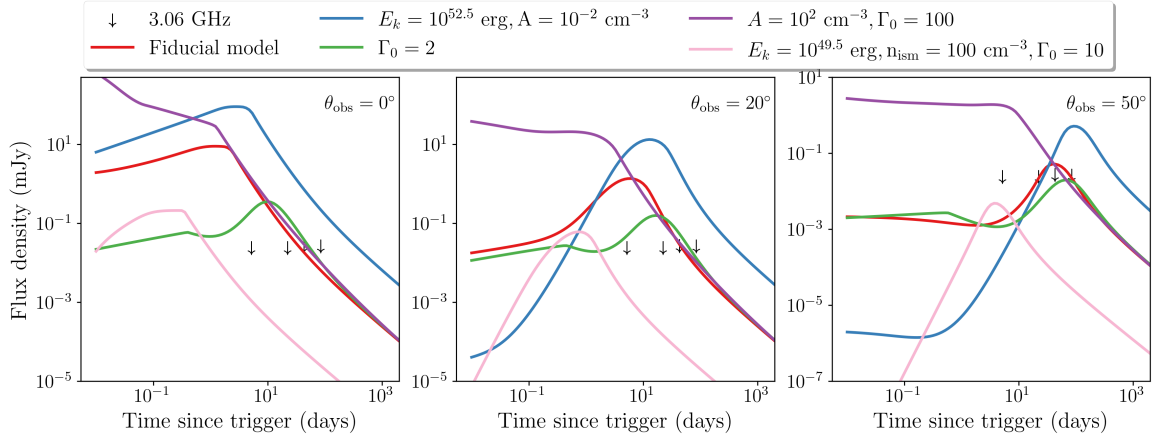
$$M_{\text{wind,enclosed}}(R) = (\dot{M}_{\text{wind}}/v_{\text{wind}})R, \quad (5)$$

where  $\dot{M}_{\text{wind}}$  is the wind mass-loss rate,  $v_{\text{wind}} \approx 1000 \text{ km s}^{-1}$ , and  $R$  is the radial extent. As discussed below, our optical light curves require strong shock interaction at early times (either a shell or a strong wind). For this calculation, we assume a strong wind:  $\dot{M}_{\text{wind}} = 10^{-4} M_{\odot} \text{ yr}^{-1}$ . We approximate the expansion velocity by applying momentum conservation,

decelerating the fastest moving material and moving inward as the high-velocity blastwave propagates through the CSM. This rapid deceleration (and deposition of this high-velocity material) is required in our supernova calculations to explain the optical emission (see Section 4.2). By also including a simple gray opacity, we can calculate the position of the photosphere (optical depth  $\sim 1$ ) and the velocity at that photosphere. Figure 11 shows this photospheric velocity evolution with time for our best-fit X-ray models (both jet driven and convective engines) from Figure 10. Although the photospheric velocity in our convective-engine model is initially slower, the larger high-velocity ejecta mass means that it decelerates slowly with time and therefore the velocity is too high to match the data at a day or so (see Section 4.2). In comparison, the low-mass jet-driven models do decelerate sufficiently quickly. We thus conclude this event is most likely powered by a collapsar engine, with the explosion driven by an accretion disk and jet. The rapid dropoff in the X-ray luminosity at late times provides a final constraint on the jet-driven models. A fraction of these models have X-ray luminosities in excess of  $10^{43} \text{ erg s}^{-1}$  at  $10^5 \text{ s}$ , inconsistent with the observed limits, and we therefore exclude them. We next explore whether we can constrain whether the jet successfully broke through the star/CSM.

#### 4.4. Constraints on Jet/ejecta Behavior

Having shown how a jet-driven engine can produce the X-ray emission observed by EP, we further examine the



**Figure 12.** Radio afterglows at 3.06 GHz following a “top-hat” jet for different assumptions of the fiducial model indicated by the red curves. The three panels correspond to different observer viewing angles while the arrows indicate upper limits from our radio observations.

constraints on its behavior from other observations. In addition to the energy limitation from the lack of gamma-ray detections (see Section 4.1), our radio observations also provide some constraints on the presence of any other fast-moving ejecta.

In Figure 12, we show the predicted radio light curves for different parameters for jets viewed on axis and  $20^\circ$  and  $50^\circ$  off axis in first, middle, and last panels, respectively. All models assume a “top-hat” jet following JETSIMPY (H. Wang et al. 2024) using REDBACK (N. Sarin et al. 2024). We note that these models do not include synchrotron self-absorption. However, this, or using a structured jet instead of a top hat, does not appreciably impact our interpretation, as the dominant uncertainty is from the parameters themselves. The black arrows indicate upper limits from our radio observations at 3.06 GHz, while the different colors indicate different assumptions about the jet parameters. The fiducial model shown in red shows the radio afterglow at 3.06 GHz of a  $10^{51.5}$  erg kinetic energy jet with an initial Lorentz factor of 1000 and  $\theta_j = 10^\circ$ , traveling into a wind medium with interstellar medium (ISM) density following  $n_{\text{ISM}} = A \left( \frac{r}{10^{17} \text{ cm}} \right)^{-2}$  where  $A = 1 \text{ cm}^{-3}$ , i.e., the density at a radius of  $10^{17}$  cm, with typical values for the microphysical parameters  $p = 2.17$ ,  $\epsilon_e = 0.1$ , and  $\epsilon_B = 0.01$ . Different colors indicate different assumptions in this fiducial model, with the pink curve representing light curves from a constant density ISM with no wind. Our radio observations can confidently rule out jets with kinetic energies  $\gtrsim 10^{51}$  erg in a wind-like medium, even for far off-axis scenarios, with the only viable solution where such a jet has a low initial Lorentz factor ( $\sim 2$ ) and also observed at least  $50^\circ$  off axis (green curves in last panel). Our nondetections cannot rule out on- or off-axis jets weaker than  $10^{50}$  erg propagating into a low-density ISM.

The radio limits from G. P. Srinivasaragavan et al. (2025) and W. X. Li et al. (2025) are also broadly consistent with our results. G. P. Srinivasaragavan et al. (2025) also model possible afterglows but assume a constant density medium as opposed to the wind medium we assume here. They also conclude a low-energy on-axis jet is plausible, but suggest that higher-energy off-axis jets may also be possible and would be expected to peak at late times.

While the above only considers jets, our results are broadly applicable to any quasi-spherical outflow such as the fast ejecta from the supernova as implied by our X-ray modeling

above. We do note, however, that our constraints are inconsistent with the slowly coasting jet suggested by W. X. Li et al. (2025) to explain the early optical emission.

#### 4.5. Origin of the Early Optical Emission

Our blackbody analyses show that we can broadly match the optical emission with a fast-moving, cooling blackbody. Here, we explore more physically motivated models. The broad similarity of our light curves to past GRBs and supernovae e.g., SN 2020bvc, provides some hints toward the appropriate models, i.e., some form of shock breakout and cooling from supernova ejecta expanding out into a dense CSM. This could be the envelope of the star, eruptive mass loss in the years leading up to the supernova, or winds from the progenitor.

We explore these different scenarios further by fitting the data for  $t \leq 6.5$  days with models for shock cooling (A. L. Piro et al. 2021) and dense CSM shell shock cooling (B. Margalit 2022) implemented in REDBACK (N. Sarin et al. 2024) using the PYMULTINEST (J. Buchner et al. 2014) via BILBY (G. Ashton et al. 2019). We fit assuming a Gaussian likelihood with a systematic error added in quadrature to the statistical errors on all data points, i.e.,  $\sigma_i^2 = \sigma_{i,\text{data}}^2 + \sigma_{\text{sys}}^2$ , where the first term is the original error on our data points and  $\sigma_{\text{sys}} = 0.15$  is a systematic uncertainty to capture any discrepancies caused by differences in photometric reduction or filter transmission curves, and broad uniform priors. We also assume the contribution from the supernova to be relatively negligible at this time as there is little evidence of plateauing or rising in the light curve. In addition, the uncertainties in the models themselves are notably larger than the possible supernova contribution. We note the key difference between the models we investigate here is the assumed profile of the CSM, with the A. L. Piro et al. (2021) model assuming a broken power-law density profile aimed to resemble homologous expansion of material following shock breakout from the star (e.g., C. D. Matzner & C. F. McKee 1999), while the later assumes a CSM shell located at initial radius,  $R_0$  of width  $\Delta R_0$ , with a sharp drop in density at larger radii, with further differences in the treatment of radiative diffusion (B. Margalit 2022).

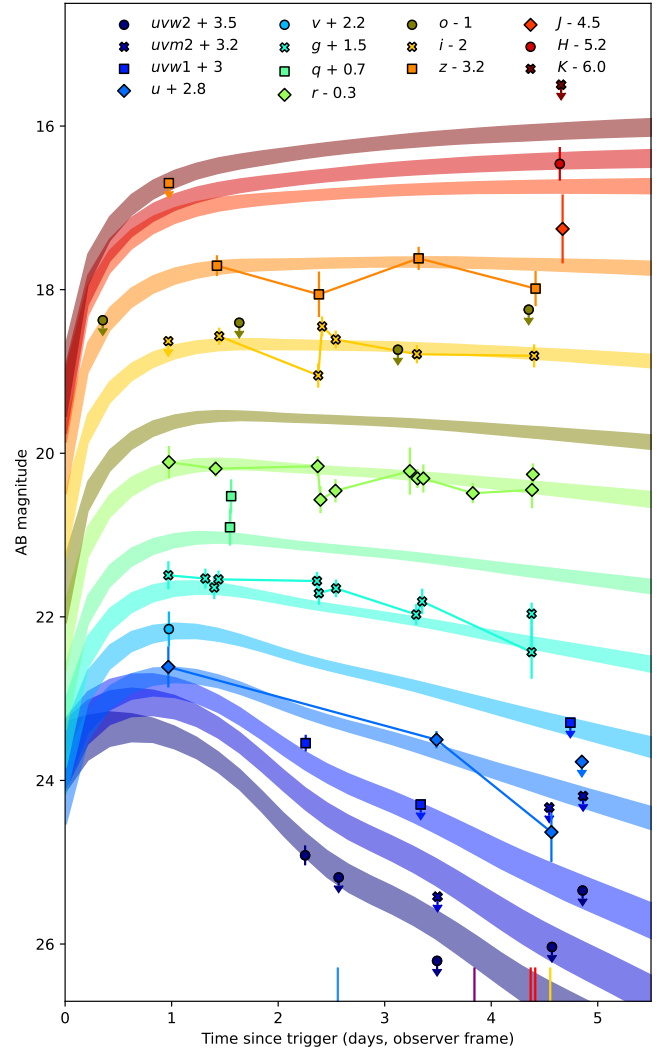
Both models capture the evolution of the light curve, however, the estimated parameters from the shock cooling model (A. L. Piro et al. 2021) are inconsistent with expectations and

our analysis of the X-ray emission, such as the overall energetics and velocities. In particular, our inference with this model suggests  $\geq 10^{52}$  erg of energy and a total CSM mass of  $\geq 6 M_{\odot}$ . We note that this is significantly larger than that found by G. P. Srinivasaragavan et al. (2025), likely due to them including an additional supernova contribution in their fit. In contrast, the dense CSM model provides more reasonable estimates consistent with the X-ray, with a CSM mass of  $0.2\text{--}0.9 M_{\odot}$ , a kinetic energy of  $\lesssim 10^{51}$  erg, with  $R_0 \sim 7 \times 10^{14}$  cm and a shell width of  $\sim 0.3 R_0$ . Our results suggest that if the light curve is powered by some form of CSM interaction, the CSM has an abrupt drop in density to adequately describe the light curve and be consistent with inferences from the X-ray observations. We note that while the model formally assumes the presence of a shell at  $R_0$ , the model is also compatible with the assumption of a wind, provided the wind is truncated at  $r > R_0$ . This provides some clues into the progenitor and perhaps a binary companion (as the CSM need not be from the progenitor of EP250108a), requiring either eruptive mass loss in the years leading up to the supernova that could place a dense CSM shell at  $R_0 \sim 10^4 R_{\odot}$  or a wind profile that terminates at such a radius.

Motivated by our X-ray analyses, which suggest that jet-driven models are most likely, we also explore a shocked cocoon/failed GRB jet model. We broadly follow the models for shocked cocoon emission outlined E. Nakar & T. Piran (2017) and A. L. Piro & J. A. Kollmeier (2018). In particular, we assume a GRB jet of negligible mass propagates out through ejecta of total mass  $M$ , with a mass profile which follows a power-law distribution:

$$m(>v) = M \left( \frac{v}{v_0} \right)^{-(s+1)}, \quad (6)$$

where  $v_0$  is the minimum velocity of the ejecta, and  $s$  is the power-law exponent of the energy distribution with respect to the velocity. The energy provided by this interaction is  $E \propto \frac{mvR}{t}$  where  $t$  is time, while the luminosity is  $\approx E(t)/t_{\text{diff}}$  where  $t_{\text{diff}}$  is the characteristic diffusion timescale. We fit this model using REDBACK with the same likelihood and data treatment as described above, further assuming that the shocked ejecta are confined to some angle  $\theta_{\text{cocoon}}$ . Our fits to the light curve are shown in Figure 13. We infer that the cocoon contains  $\sim 0.04\text{--}0.15 M_{\odot}$  of shocked ejecta, confined to  $\sim 20^{\circ}\text{--}25^{\circ}$ , with a kinetic energy of  $\sim 4\text{--}45 \times 10^{50}$  erg and a shock radius of  $\sim 1.9\text{--}3.5 R_{\odot}$ . This model provides a good fit to the data, and our parameters are broadly in agreement with inferences from the X-ray observations and the constraints from the radio observations above. They are also consistent with the results of G. P. Srinivasaragavan et al. (2025) who fit a similar model. While we cannot definitively rule out whether any jet successfully broke out, the inferred energetics from our modeling above as well as the radio and X-rays constraints suggest that if EP250108a/SN 2025kg was jet driven, either no jet broke out or it was weaker than  $\approx 10^{51}$  erg. We note that, here we only considered the thermal emission from the shocked cocoon. Such shocked cocoons are also expected to produce nonthermal emission as discussed earlier in Section 4. However, this is extremely sensitive to assumptions about microphysical parameters and the quantity of fast ejecta, which our modeling here does not constrain.



**Figure 13.** The UVOIR light curve of SN 2025kg’s fast cooling phase fitted with a shocked cocoon model. The shaded regions indicate the 68% credible interval of the posterior predictive distribution for each band. The vertical lines indicate the times of our spectroscopic observations (with colors corresponding to Figure 4).

## 5. Conclusions

In this letter, we have detailed our observations and analysis of the fast cooling phase of EP250108a/SN 2025kg, comprising the first  $\sim 6$  days of data. We have also used X-ray and radio data from later times to further investigate the transient. The remaining data from our campaign and its analysis are presented in J. C. Rastinejad et al. (2025), who examine the properties of the supernova itself in much greater detail. We summarize our conclusions below.

1. SN 2025kg’s early evolution shows distinct similarity to similar behavior in the Type Ic-BL SN 2006aj and SN 2020bvc suggesting these events arise from similar progenitor systems. There are also similarities to early features in other Type Ic-BL supernovae SN 2017iuk and possibly SN 2024gsa. In our companion Letter, J. C. Rastinejad et al. (2025), we show the properties of SN 2006aj, SN 2020bvc, and SN 2024gsa are also similar.
2. We find that the optical transient is consistent with an expanding, cooling blackbody similar to several other

examples in the GRB-SN population, in particular SN 2006aj and SN 2020bvc. We simulate the photometry using this model and find, by extrapolation, an initial expansion velocity of order  $\sim 0.4\text{--}0.6c$  that later declines to  $\sim 0.1\text{--}0.2c$  by about 0.5 days (rest frame).

3. The X-ray emission likely arises from a jet-driven engine. To achieve the deceleration and rapid fading required from the observed data, a convection engine would require both extreme supernova energies and masses. However, the low masses required by a collapsar jet engine allow this rapid deceleration and decline in luminosity. The limits set by our radio observations and Fermi gamma-ray observations indicate the jet is low energy and/or failed to successfully break out, assuming top-hat jets in a wind medium. We cannot, at this point, constrain whether we are viewing the jet off axis.
4. These results suggest that the optical transient is driven by either shock cooling as supernova ejecta expand into a dense shell of CSM or the jet inferred from the X-rays propagates through the ejecta to produce a shocked cocoon. Both models are consistent with the data and support the suggestion that the jet was low energy or failed to successfully break out. Our conclusions are consistent with the findings of G. P. Srinivasaragavan et al. (2025) and W. X. Li et al. (2025). In J. C. Rastinejad et al. (2025), we further discuss the progenitor system and rates of these failed/weak jet powered FXT-SNe and show that they are likely higher than similar GRB-SNe.

Despite similarities to previous supernova, SN 2025kg is an extraordinary source in terms of both physics and the quality of the data produced by both us and other groups (W. X. Li et al. 2025d; G. P. Srinivasaragavan et al. 2025). EP and its unique ability to identify FXTs in real time will allow many more of these rare events to be uncovered and the exact physics underpinning them to be explored.

### Acknowledgments

We are deeply grateful to Tom Marsh for developing the MOLLY software, one of his many contributions to advancing the field of compact objects.

We thank Genevieve Schroeder and Gokul Prem Srinivasaragavan for useful discussion.

We also thank the anonymous referee for their constructive comments that improved our original manuscript.

The Liverpool Telescope is operated on the island of La Palma by Liverpool John Moores University in the Spanish Observatorio del Roque de los Muchachos of the Instituto de Astrofísica de Canarias with financial support from the UK Science and Technology Facilities Council.

The data presented here were obtained in part with ALFOSC, which is provided by the Instituto de Astrofísica de Andalucía (IAA) under a joint agreement with the University of Copenhagen and NOT.

This work is partly based on observations collected at the European Southern Observatory under ESO program 114.27PZ.001.

This work is partly based on observations made with the Gran Telescopio Canarias (GTC), installed at the Spanish Observatorio del Roque de los Muchachos of the Instituto de Astrofísica de Canarias, on the island of La Palma, under program GTC1-24ITP. These data were obtained with the

instrument OSIRIS, built by a Consortium led by the Instituto de Astrofísica de Canarias in collaboration with the Instituto de Astronomía of the Universidad Autónoma de México. OSIRIS was funded by GRANTECAN and the National Plan of Astronomy and Astrophysics of the Spanish Government.

This work is partly based on observations obtained at the international Gemini Observatory, a program of NSF NOIR-Lab, which is managed by the Association of Universities for Research in Astronomy (AURA) under a cooperative agreement with the U.S. National Science Foundation on behalf of the Gemini Observatory partnership: the U.S. National Science Foundation (United States), National Research Council (Canada), Agencia Nacional de Investigación y Desarrollo (Chile), Ministerio de Ciencia, Tecnología e Innovación (Argentina), Ministério da Ciência, Tecnologia e Inovações e Comunicações (Brazil), and Korea Astronomy and Space Science Institute (Republic of Korea), under programs GN-2024B-Q-107 and GS-2024B-Q-105.

This work made use of data supplied by the UK Swift Science Data Centre at the University of Leicester.

Data for this Letter has in part been obtained under the International Time Programme of the CCI (International Scientific Committee of the Observatorios de Canarias of the IAC) with the NOT and GTC operated on the island of La Palma by the Roque de los Muchachos.

This work makes use of observations using the Sinistro imager on the LCOGT 1 m telescope at the South African Astronomical Observatory.

The MeerKAT telescope is operated by the South African Radio Astronomy Observatory, which is a facility of the National Research Foundation, an agency of the Department of Science and Innovation. This work has made use of the “MPIfR S-band receiver system” designed, constructed, and maintained by funding of the MPI für Radioastronomie and the Max Planck Society.

Based on observations with the BlackGEM telescope array. The BlackGEM telescope array is built and run by a consortium consisting of Radboud University, the Netherlands Research School for Astronomy (NOVA), and KU Leuven with additional support from Armagh Observatory and Planetarium, Durham University, Hamburg Observatory, Hebrew University, Las Cumbres Observatory, Tel Aviv University, Texas Tech University, Technical University of Denmark, University of California Davis, the University of Barcelona, the University of Manchester, University of Potsdam, the University of Valparaíso, the University of Warwick, and Weizmann Institute of science. BlackGEM is hosted and supported by ESO at La Silla.

P.G.J., M.E.R., and J.N.D.vD. are funded by the European Union (ERC, Starstruck, 101095973). Views and opinions expressed are however those of the authors only and do not necessarily reflect those of the European Union or the European Research Council Executive Agency. Neither the European Union nor the granting authority can be held responsible for them. N.S. acknowledges support from the Knut and Alice Wallenberg Foundation through the “Gravity Meets Light” project and the research environment grant “Gravitational Radiation and Electromagnetic Astrophysical Transients” (GREAT) funded by the Swedish Research Council (VR) under Dnr 2016-06012. The work by C.L.F. was supported by the US Department of Energy through the Los Alamos National Laboratory. Los Alamos National



Laboratory is operated by Triad National Security, LLC, for the National Nuclear Security Administration of U.S. Department of Energy (contract No. 89233218CNA000001). P.T.O. acknowledges support from UKRI under grant ST/W000857/1. B.P.G. acknowledges support from STFC grant No. ST/Y002253/1 and The Leverhulme Trust grant No. RPG-2024-117. A.S. acknowledges support by a postdoctoral fellowship from the CNES. R.L.C.S. acknowledges support from Leverhulme Trust grant RPG-2023-240. G.L. is supported by a research grant (VIL60862) from VILLUM FONDEN. D.M.S. and M.A.P.T. acknowledge support by the Spanish Ministry of Science via the Plan de Generacion de conocimiento PID2020-120323GB-I00. D.M.S. also acknowledges support via a Ramon y Cajal Fellowship RYC2023-044941. C.J.N. acknowledges support from the Science and Technology Facilities Council (grant No. ST/Y000544/1) and from the Leverhulme Trust (grant No. RPG-2021-380).

For the purpose of open access, the author has applied a Creative Commons Attribution (CC BY) licence to the Author Accepted Manuscript version arising from this submission.

*Facilities:* Gemini:Gillett (GMOS-N), Gemini:South (FLAMINGOS2), GTC (OSIRIS), LCOGT (SINISTRO), Liverpool:2m (IO:O), NOT (ALFOSC), Swift (XRT and UVOT), VLT:Melipal (X-shooter).

*Software:* astropy (Astropy Collaboration et al. 2013, 2018, 2022), dust\_extinction (K. Gordon 2024), emcee (D. Foreman-Mackey et al. 2013), ESOREFLEX (W. Freudling et al. 2013), HEASOFT (Nasa High Energy Astrophysics Science Archive Research Center (Heasarc) 2014), photometry-sans-frustration (M. Nicholl et al. 2023), PIMMS, PyZOGY (D. Guevel et al. 2021), REDBACK (N. Sarin et al. 2024).

## Appendix A Observing Logs

In this Appendix, we present our observing logs of EP250108a/SN 2025kg. In Table 3, we present our UV, optical, and infrared photometry. We summarise our spectroscopic observations and subsequent analysis in Table 4. Finally in Tables 5 and 6, we present our X-ray and radio observations.

**Table 3**  
The Assembled Ultraviolet, Optical, and Near-infrared Photometry from Our Observations and Other Sources

Date (UT)	$\Delta t$ (days)	Instrument	Filter	Exposure Time (s)	AB Magnitude	References
2025 Jan 10.77415	2.25299	Swift/UVOT	<i>uvw2</i>	1007.4	$21.55 \pm 0.07$	Revision of A. J. Levan et al. (2025a)
2025 Jan 11.08888	2.56773	Swift/UVOT	<i>uvw2</i>	1080.2	$>21.82$	This work
2025 Jan 12.01286	3.49171	Swift/UVOT	<i>uvw2</i>	2053.3	$>22.84$	This work
2025 Jan 13.09120	4.57005	Swift/UVOT	<i>uvw2</i>	1667.2	$>22.67$	This work
2025 Jan 13.37897	4.85782	Swift/UVOT	<i>uvw2</i>	597.2	$>21.98$	This work
2025 Jan 12.01700	3.49584	Swift/UVOT	<i>uvm2</i>	917.4	$>22.37$	This work
2025 Jan 13.06583	4.54467	Swift/UVOT	<i>uvm2</i>	215.0	$>21.28$	This work
2025 Jan 13.38372	4.86257	Swift/UVOT	<i>uvm2</i>	198.8	$>21.14$	This work
2025 Jan 10.77958	2.25842	Swift/UVOT	<i>uvw1</i>	843.9	$20.65 \pm 0.02$	Revision of A. J. Levan et al. (2025a)
2025 Jan 11.85942	3.33827	Swift/UVOT	<i>uvw1</i>	251.2	$>21.40$	This work
2025 Jan 13.26392	4.74277	Swift/UVOT	<i>uvw1</i>	67.6	$>20.40$	This work
2025 Jan 09.49019	0.969	MEPHISTO	<i>u</i> <sup>a</sup>	$2 \times 180$	$19.89 \pm 0.23$	X. Zou et al. (2025)
2025 Jan 12.00747	3.48631	Swift/UVOT	<i>u</i>	2892.0	$20.78 \pm 0.03$	This work
2025 Jan 13.08614	4.56499	Swift/UVOT	<i>u</i>	2744.4	$21.91 \pm 0.35$	This work
2025 Jan 13.37186	4.85071	Swift/UVOT	<i>u</i>	597.2	$>21.05$	This work
2025 Jan 09.41519	0.974	MEPHISTO	<i>v</i>	$2 \times 180$	$20.02 \pm 0.19$	X. Zou et al. (2025)
2025 Jan 06.20545	-2.31571	ZTF	<i>g</i>	30	$>21.54$	This work
2025 Jan 09.49020	0.969	MEPHISTO	<i>g</i>	$6 \times 50$	$20.05 \pm 0.14$	X. Zou et al. (2025)
2025 Jan 09.83781	1.31665	LT/IO:O	<i>g</i>	$1 \times 200$	$20.09 \pm 0.07$	Revision of R. A. J. Eyles-Ferris (2025)
2025 Jan 9.920945	$\sim 1.4$	LT/IO:O	<i>g</i>	...	$20.20 \pm 0.10$	A. Kumar et al. (2025)
2025 Jan 9.96101	1.43985	NOT/ALFOSC	<i>g</i>	$2 \times 300$	$20.10 \pm 0.04$	Revision of Z. P. Zhu et al. (2025a)
2025 Jan 10.19027	1.66912	ZTF	<i>g</i>	30	$>19.00$	This work
2025 Jan 10.88571	2.36454	NOT/ALFOSC	<i>g</i>	$2 \times 300$	$20.12 \pm 0.05$	D. B. Malesani et al. (2025)
2025 Jan 10.90305	2.38189	LT/IO:O	<i>g</i>	$6 \times 200$	$20.27 \pm 0.10$	This work
2025 Jan 11.06419	2.54302	VLT/X-shooter	<i>g</i>	$3 \times 40$	$20.21 \pm 0.04$	This work
2025 Jan 11.81677	3.29560	NOT/ALFOSC	<i>g</i>	$2 \times 300$	$20.53 \pm 0.08$	This work
2025 Jan 11.87469	3.35160	LCO/Sinistro	<i>g</i>	$3 \times 300$	$20.37 \pm 0.12$	Revision of L. Izzo (2025)
2025 Jan 12.16815	3.64700	ZTF	<i>g</i>	30	$>19.01$	This work
2025 Jan 12.90017	4.37901	LCO/Sinistro	<i>g</i>	$3 \times 300$	$20.99 \pm 0.31$	This work
2025 Jan 12.90049	4.37933	LT/IO:O	<i>g</i>	$6 \times 150$	$20.52 \pm 0.09$	This work
2025 Jan 13.18974	4.66859	ZTF	<i>g</i>	30	$>19.63$	This work
2025 Jan 10.06904	1.54788	BlackGEM	<i>q</i>	60	$20.25 \pm 0.20$	This work
2025 Jan 10.07963	1.55847	BlackGEM	<i>q</i>	60	$19.87 \pm 0.18$	This work

**Table 3**  
(Continued)

Date (UT)	$\Delta t$ (days)	Instrument	Filter	Exposure Time (s)	AB Magnitude	References
2025 Jan 09.41519	0.974	MEPHISTO	<i>r</i>	$6 \times 50$	$20.45 \pm 0.17$	X. Zou et al. (2025)
2025 Jan 9.93392	1.41277	NOT/ALFOSC	<i>r</i>	$3 \times 300$	$20.53 \pm 0.02$	Revision of Z. P. Zhu et al. (2025a)
2025 Jan 10.89215	2.37098	NOT/ALFOSC	<i>r</i>	$2 \times 180$	$20.50 \pm 0.07$	D. B. Malesani et al. (2025)
2025 Jan 10.91841	2.39725	LT/IO:O	<i>r</i>	$6 \times 200$	$20.91 \pm 0.13$	This work
2025 Jan 11.05948	2.53831	VLT/X-shooter	<i>r</i>	$3 \times 30$	$20.80 \pm 0.10$	This work
2025 Jan 11.75736	3.2362	SAO RAS Zeis-1000	<i>r</i>	$8 \times 300$	$20.56 \pm 0.27$	A. S. Moskvitin et al. (2025)
2025 Jan 11.82939	3.30822	NOT/ALFOSC	<i>r</i>	$3 \times 180$	$20.65 \pm 0.06$	This work
2025 Jan 11.88624	3.363	LCO/Sinistro	<i>r</i>	$3 \times 300$	$20.65 \pm 0.14$	Revision of L. Izzo (2025).
2025 Jan 12.23224	3.71109	ZTF	<i>r</i>	30	$>19.58$	This work
2025 Jan 12.34830	3.82715	Gemini-North/GMOS-N	<i>r</i>	50	$20.83 \pm 0.07$	This work
2025 Jan 12.90408	4.38292	LCO/Sinistro	<i>r</i>	$3 \times 300$	$20.79 \pm 0.20$	This work
2025 Jan 12.91241	4.39125	LT/IO:O	<i>r</i>	$6 \times 150$	$20.60 \pm 0.09$	This work
2025 Jan 13.21237	4.69121	ZTF	<i>r</i>	30	$>19.06$	This work
2025 Jan 08.87477	0.35362	ATLAS	<i>o</i>	$3 \times 30$	$>19.41$	This work
2025 Jan 10.15593	1.63478	ATLAS	<i>o</i>	$4 \times 30$	$>19.44$	This work
2025 Jan 11.64527	3.12411	ATLAS	<i>o</i>	$6 \times 30$	$>19.77$	This work
2025 Jan 12.87307	4.35191	ATLAS	<i>o</i>	$4 \times 30$	$>19.28$	This work
2025 Jan 14.12614	5.60499	ATLAS	<i>o</i>	$3 \times 30$	$>19.10$	This work
2025 Jan 09.49020	0.969	MEPHISTO	<i>i</i>	$4 \times 79$	$>20.66$	X. Zou et al. (2025)
2025 Jan 9.96796	1.44681	NOT/ALFOSC	<i>i</i>	$2 \times 180$	$20.60 \pm 0.03$	Revision of Z. P. Zhu et al. (2025a)
2025 Jan 10.89718	2.37601	NOT/ALFOSC	<i>i</i>	$2 \times 180$	$21.08 \pm 0.11$	D. B. Malesani et al. (2025)
2025 Jan 10.93375	2.41259	LT/IO:O	<i>i</i>	$6 \times 200$	$20.48 \pm 0.07$	This work
2025 Jan 11.06172	2.54056	VLT/X-shooter	<i>i</i>	$3 \times 60$	$20.64 \pm 0.04$	This work
2025 Jan 11.82321	3.30204	NOT/ALFOSC	<i>i</i>	$2 \times 180$	$20.82 \pm 0.05$	This work
2025 Jan 12.92426	4.4031	LT/IO:O	<i>i</i>	$6 \times 150$	$20.84 \pm 0.10$	This work
2025 Jan 09.49519	0.974	MEPHISTO	<i>z</i>	$4 \times 79$	$>19.92$	X. Zou et al. (2025)
2025 Jan 9.94647	1.4253	NOT/ALFOSC	<i>z</i>	$5 \times 200$	$20.93 \pm 0.08$	Revision of Z. P. Zhu et al. (2025a)
2025 Jan 10.90377	2.3826	NOT/ALFOSC	<i>z</i>	$3 \times 200$	$21.28 \pm 0.26$	D. B. Malesani et al. (2025)
2025 Jan 11.83977	3.3186	NOT/ALFOSC	<i>z</i>	$5 \times 200$	$20.84 \pm 0.10$	This work
2025 Jan 12.93758	4.41642	LT/IO:O	<i>z</i>	$6 \times 200$	$21.21 \pm 0.19$	This work
2025-01-13 4:35:25	4.67009	Gemini-South/F2	<i>J</i>	$3 \times 30$	$21.77 \pm 0.41$	This work
2025-01-13 3:57:32	4.64378	Gemini-South/F2	<i>H</i>	$25 \times 15$	$21.67 \pm 0.18$	This work
2025-01-13 4:15:23	4.65618	Gemini-South/F2	<i>K</i>	$24 \times 15$	$>21.50$	This work

**Note.**  $\Delta t$  is given in the observer frame and magnitudes are as measured and are not corrected for Galactic extinction.

<sup>a</sup> The effective wavelengths of the MEPHISTO *u* and Swift/UVOT *u* filters are separated by approximately 35 Å. In this work we assume them to have the same effective wavelength of 3483 Å.

**Table 4**  
The Log of Our Spectroscopic Observations

Date (UT)	$\Delta t$ (days)	Instrument	Exposure Time (s)	$T_{\text{bb}}$ ( $10^4$ K)	$R_{\text{bb}}$ ( $10^{15}$ cm)	$\log \left( \frac{L_{\text{bb,bol}}}{\text{erg s}^{-1}} \right)$
2025 Jan 11.08112	2.56000	VLT/X-shooter	$4 \times 600$	$1.23 \pm 0.01$	$1.13 \pm 0.01$	$43.32 \pm 0.01$
2025 Jan 12.36373	3.84257	Gemini-North/GMOS-N	$3 \times 400$	$1.17 \pm 0.04$	$1.04 \pm 0.05$	$43.17 \pm 0.02$
2025 Jan 12.89132	4.37016	GTC/OSIRIS+/R1000R <sup>a</sup>	$3 \times 1200$	$1.24 \pm 0.02$	$1.12 \pm 0.02$	$43.33 \pm 0.01$
2025 Jan 12.93447	4.41331	GTC/OSIRIS+/R1000B <sup>a</sup>	$3 \times 1200$	$1.24 \pm 0.02$	$1.12 \pm 0.02$	$43.33 \pm 0.01$
2025 Jan 13.07514	4.55398	VLT/X-shooter	$4 \times 600$	$0.96 \pm 0.01$	$1.34 \pm 0.02$	$43.04 \pm 0.01$

**Notes.**  $\Delta t$  is given in the observer frame.

<sup>a</sup> Note that we combine the data from the two GTC/OSIRIS+ observations to produce a single spectrum covering the full wavelength range of both gratings.

**Table 5**  
The Log of Our X-Ray Observations and Additional Public Data Observed by Swift

Date (UT)	$\Delta t$ (days)	Instrument	Exposure Time (ks)	$\log \left( \frac{L_{0.5-10 \text{ keV}}}{\text{erg s}^{-1}} \right)$
2025 Jan 10.86591	2.34475	Swift/XRT	2.989	<42.65
2025 Jan 12.01331	3.49215	Swift/XRT	4.919	<42.45
2025 Jan 13.12290	4.60175	Swift/XRT	5.139	<42.57
2025 Jan 14.72557	6.20441	XMM-Newton/pn	30.44	<40.99
2025 Jan 23.16258	14.64143	Swift/XRT	1.59	<42.74
2025 Jan 23.32540	14.80424	Swift/XRT	1.248	<43.03
2025 Jan 28.85781	20.33665	Chandra/ACIS-S3	10.851	<41.66

**Note.**  $\Delta t$  is given in the observer frame.

**Table 6**  
The Log of Our Radio Observations

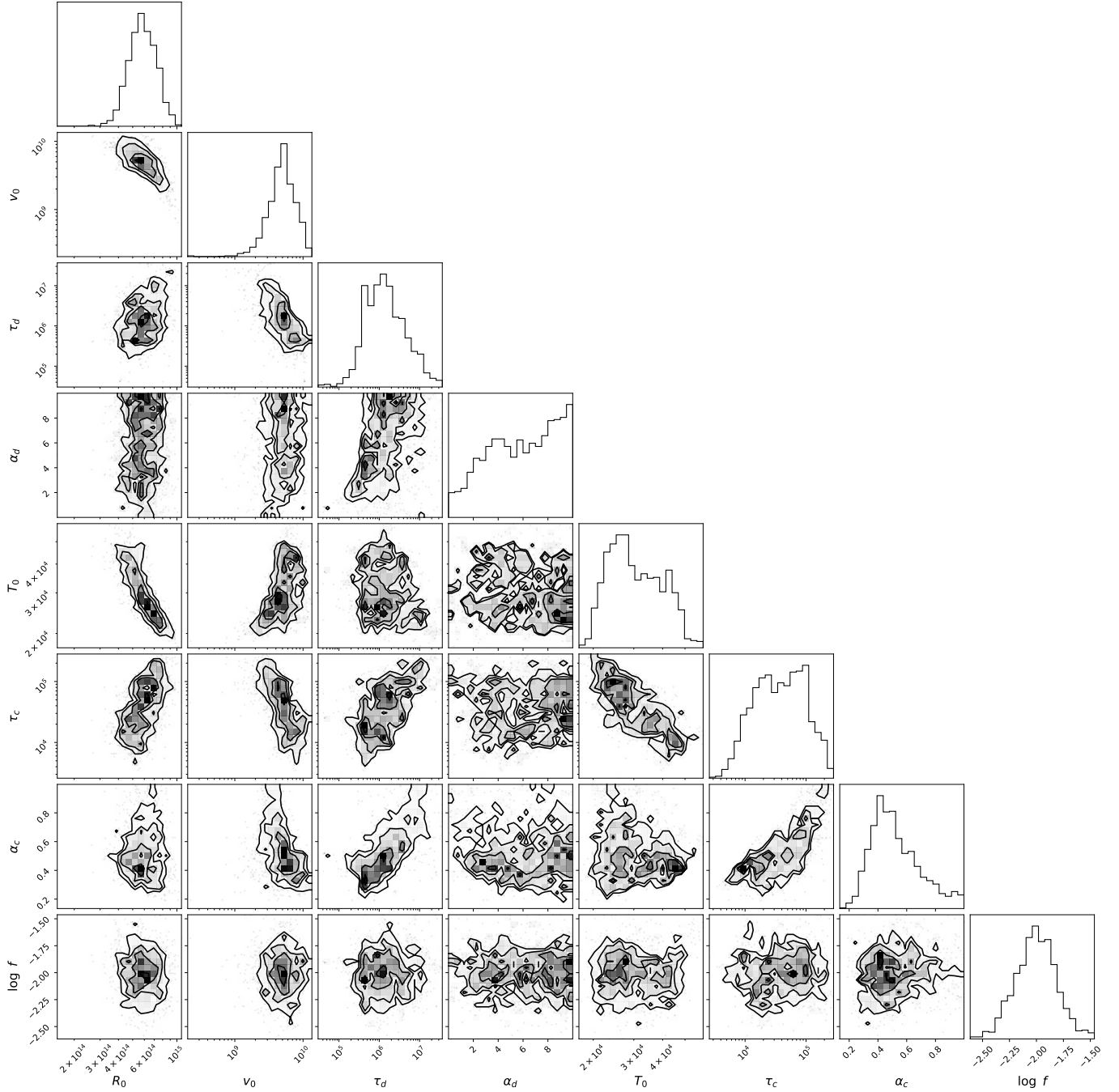
Date (UT)	$\Delta t$ (days)	Telescope	Central Frequency (GHz)	Integration Time (minutes)	$F_\nu$ ( $\mu\text{Jy beam}^{-1}$ )
2025 Jan 13.74792	5.22676	MeerKAT	3.06	42	24
2025 Jan 30.57014	22.04898	MeerKAT	3.06	42	24
2025 Feb 20.66319	43.14203	MeerKAT	3.06	42	27
2025 Apr 3.39167	84.87051	MeerKAT	3.06	42	26

**Note.**  $\Delta t$  is given in the observer frame.

## Appendix B

### Corner Plot

In Figure 14, we show the corner plot derived from our MCMC chain when fitting the photometry with our cooling, expanding blackbody model (see Section 4.2.).



**Figure 14.** A corner plot showing the parameter covariance in our fit to SN 2025kg's fast cooling phase with a cooling, expanding blackbody.



### Appendix C

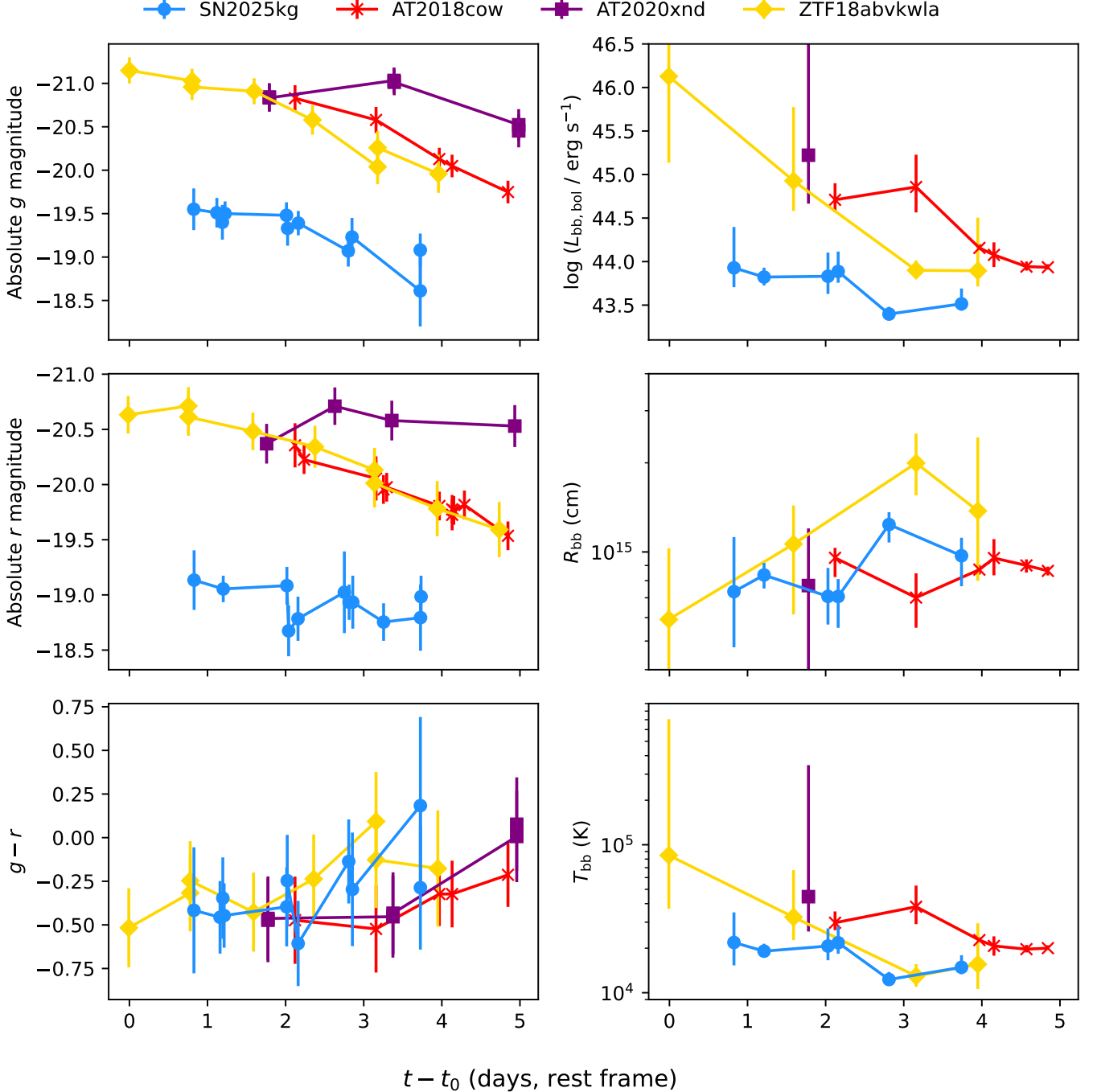
#### SN 2025kg in Relation to Luminous Fast Blue Optical Transients

Another class of transients that also display a blue color with rapid temperature and luminosity evolution is LFBOTs. Initially, SN 2025kg was suggested to be a member of this class (Z. P. Zhu et al. 2025b) while a link has also been suggested in the case of the FXT supernova SN 2024gsa (J. N. D. van Dalen et al. 2025). Here we briefly consider the fast cooling phase’s properties in relation to observed LFBOTs.

In Figure 15, we compare the fast cooling phase of SN 2025kg to early data from AT2018cow (R. Margutti et al. 2019;

D. A. Perley et al. 2019; S. J. Prentice et al. 2018), ZTF18abvkwla (A. Y. Q. Ho et al. 2020b), and AT2020xnd/ZTF20acigmel (D. A. Perley et al. 2021; J. S. Bright et al. 2022; A. Y. Q. Ho et al. 2022a). Additional examples include AT2020mrf (Y. Yao et al. 2022) and AT2022tsd (A. Y. Q. Ho et al. 2022a, 2022c; D. Matthews et al. 2023). Similarly to our supernova comparison above, blackbodies are fitted to individual epochs of the cataloged photometry using the procedure in Section 2.1.

From Figure 15, it is clear that from the optical properties alone, SN 2025kg is very different to behavior observed in the LFBOT population. In particular, it is less luminous and cooler than both the prototypical AT2018cow and AT2020xnd. The














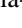




**Figure 15.** The photometric and blackbody properties of SN 2025kg’s fast cooling phase compared to the early properties of the LFBOTs AT2018cow, ZTF18abvkwla, and AT2020xnd. Note that we have taken  $t_0 = 58374.41$  MJD for ZTF18abvkwla, i.e., the peak time in the  $g$ -band light curve.

blackbody radius of SN 2025kg is also somewhat larger and continuing to expand. While Figure 15 only shows the earliest times, both LFBOTs' photospheres were shown to recede. Extending the comparison to other wavelengths, the rapid fading of EP250108a is also inconsistent with the X-ray behavior of both of these events, which display emission over tens of days at luminosities incompatible with the upper limits we derive above. At this time cannot rule out similar behavior to that seen in another LFBOT, CSS161010 (D. L. Coppejans et al. 2020; C. P. Gutiérrez et al. 2024), which displayed lower luminosity X-ray emission at  $\sim 100$  days postoutburst. Similarly, our current radio limits for SN 2025kg are compatible with the behavior seen in the LFBOT sample, which are still rising at a comparable time.

To conclude, SN 2025kg is inconsistent with many properties of LFBOTs at optical and X-ray wavelengths and it is unlikely that the same progenitor system is responsible for producing both classes of transient.

### ORCID iDs

Rob A. J. Eyles-Ferris  <https://orcid.org/0000-0002-8775-2365>  
 Peter G. Jonker  <https://orcid.org/0000-0001-5679-0695>  
 Andrew J. Levan  <https://orcid.org/0000-0001-7821-9369>  
 Daniele Bjørn Malesani  <https://orcid.org/0000-0002-7517-326X>  
 Nikhil Sarin  <https://orcid.org/0000-0003-2700-1030>  
 Christopher L. Fryer  <https://orcid.org/0000-0003-2624-0056>  
 Jillian C. Rastinejad  <https://orcid.org/0000-0002-9267-6213>  
 Eric Burns  <https://orcid.org/0000-0002-2942-3379>  
 Nial R. Tanvir  <https://orcid.org/0000-0003-3274-6336>  
 Paul T. O'Brien  <https://orcid.org/0000-0002-5128-1899>  
 Wen-fai Fong  <https://orcid.org/0000-0002-7374-935X>  
 Ilya Mandel  <https://orcid.org/0000-0002-6134-8946>  
 Benjamin P. Gompertz  <https://orcid.org/0000-0002-5826-0548>  
 Charles D. Kilpatrick  <https://orcid.org/0000-0002-5740-7747>  
 Steven Bloemen  <https://orcid.org/0000-0002-6636-921X>  
 Joe S. Bright  <https://orcid.org/0000-0002-7735-5796>  
 Francesco Carotenuto  <https://orcid.org/0000-0002-0426-3276>  
 Gregory Corcoran  <https://orcid.org/0009-0009-1573-8300>  
 Laura Cotter  <https://orcid.org/0000-0002-7910-6646>  
 Paul J. Groot  <https://orcid.org/0000-0002-4488-726X>  
 Luca Izzo  <https://orcid.org/0000-0001-9695-8472>  
 Tanmoy Laskar  <https://orcid.org/0000-0003-1792-2338>  
 Antonio Martin-Carrillo  <https://orcid.org/0000-0001-5108-0627>  
 Jesse Palmerio  <https://orcid.org/0000-0002-9408-1563>  
 Maria E. Rivasio  <https://orcid.org/0000-0003-3193-4714>  
 Jan van Roestel  <https://orcid.org/0000-0002-2626-2872>  
 Andrea Saccardi  <https://orcid.org/0000-0002-6950-4587>  
 Rhaana L. C. Starling  <https://orcid.org/0000-0001-5803-2038>  
 Aishwarya Linesh Thakur  <https://orcid.org/0000-0001-9354-2308>  
 Susanna D. Vergani  <https://orcid.org/0000-0001-9398-4907>  
 Franz E. Bauer  <https://orcid.org/0000-0002-8686-8737>  
 Sergio Campana  <https://orcid.org/0000-0001-6278-1576>  
 Jennifer A. Chacón  <https://orcid.org/0009-0000-6374-3221>  
 Ashley A. Chrimes  <https://orcid.org/0000-0001-9842-6808>  
 Stefano Covino  <https://orcid.org/0000-0001-9078-5507>  
 Joyce N. D. van Dalen  <https://orcid.org/0009-0007-6927-7496>  
 Valerio D'Elia  <https://orcid.org/0000-0003-3703-4418>  
 Massimiliano De Pasquale  <https://orcid.org/0000-0002-4036-7419>

Nusrin Habeeb  <https://orcid.org/0009-0004-9861-8200>  
 Dieter H. Hartmann  <https://orcid.org/0000-0002-8028-0991>  
 Agnes P. C. van Hoof  <https://orcid.org/0009-0005-5404-2745>  
 Páll Jakobsson  <https://orcid.org/0000-0002-9404-5650>  
 Yashaswi Julakanti  <https://orcid.org/0000-0002-0774-2328>  
 Giorgos Leloudas  <https://orcid.org/0000-0002-8597-0756>  
 Daniel Mata Sánchez  <https://orcid.org/0000-0003-0245-9424>  
 Christopher J. Nixon  <https://orcid.org/0000-0002-2137-4146>  
 Daniëlle L. A. Pieterse  <https://orcid.org/0000-0003-3114-2733>  
 Giovanna Pugliese  <https://orcid.org/0000-0003-3457-9375>  
 Jonathan Quirola-Vásquez  <https://orcid.org/0000-0001-8602-4641>  
 Ben C. Rayson  <https://orcid.org/0009-0000-2285-8188>  
 Ruben Salvaterra  <https://orcid.org/0000-0002-9393-8078>  
 Ben Schneider  <https://orcid.org/0000-0003-4876-7756>  
 Manuel A. P. Torres  <https://orcid.org/0000-0002-5297-2683>  
 Tayyaba Zafar  <https://orcid.org/0000-0003-3935-7018>

### References

- Alp, D., & Larsson, J. 2020, *ApJ*, **896**, 39  
 An, T., Liu, Y., Geng, J., et al. 2025, *GCN*, **38998**, 1  
 Ashton, G., Hübner, M., Lasky, P. D., et al. 2019, *ApJS*, **241**, 27  
 Astropy Collaboration, Price-Whelan, A. M., Lim, P. L., et al. 2022, *ApJ*, **935**, 167  
 Astropy Collaboration, Price-Whelan, A. M., Sipőcz, B. M., et al. 2018, *AJ*, **156**, 123  
 Astropy Collaboration, Robitaille, T. P., Tollerud, E. J., et al. 2013, *A&A*, **558**, A33  
 Bauer, F. E., Treister, E., Schawinski, K., et al. 2017, *MNRAS*, **467**, 4841  
 Breeveld, A. A., Landsman, W., Holland, S. T., et al. 2011, in *AIP Conf. Ser.* 1358, *Gamma Ray Bursts 2010*, ed. J. E. McEnery, J. L. Racusin, & N. Gehrels (Melville, NY: AIP), 373  
 Bright, J. S., Margutti, R., Matthews, D., et al. 2022, *ApJ*, **926**, 112  
 Buchner, J., Georgakakis, A., Nandra, K., et al. 2014, *A&A*, **564**, A125  
 Bufano, F., Pian, E., Sollerman, J., et al. 2012, *ApJ*, **753**, 67  
 Camilo, F., Scholz, P., Serylak, M., et al. 2018, *ApJ*, **856**, 180  
 Campana, S., Lodato, G., D'Avanzo, P., et al. 2011, *Natur*, **480**, 69  
 Campana, S., Mangano, V., Blustin, A. J., et al. 2006, *Natur*, **442**, 1008  
 Cano, Z., Bersier, D., Guidorzi, C., et al. 2011, *ApJ*, **740**, 41  
 Chen, W., Wang, W. X., Zhang, Y. J., et al. 2025, *GCN*, **39580**, 1  
 Cobb, B. E., Bailyn, C. D., van Dokkum, P. G., & Natarajan, P. 2006, *ApJL*, **645**, L113  
 Coppejans, D. L., Margutti, R., Terreran, G., et al. 2020, *ApJL*, **895**, L23  
 De Luca, A., Salvaterra, R., Belfiore, A., et al. 2021, *A&A*, **650**, A167  
 Declair, M., Gordon, K. D., Andrews, J. E., et al. 2022, *ApJ*, **930**, 15  
 D'Elia, V., Campana, S., D'Ai, A., et al. 2018, *A&A*, **619**, A66  
 Dessart, L., Yoon, S.-C., Aguilera-Dena, D. R., & Langer, N. 2020, *A&A*, **642**, A106  
 Emery, S. W. K., Page, M. J., Breeveld, A. A., et al. 2019, *MNRAS*, **484**, 5484  
 Evans, P. A., Page, K. L., Beardmore, A. P., et al. 2023, *MNRAS*, **518**, 174  
 Eyles-Ferris, R. A. J. 2025, *GCN*, **38878**, 1  
 Eyles-Ferris, R. A. J., Malesani, D. B., O'Brien, P. T., et al. 2025, *GCN*, **38983**, 1  
 Ferrero, P., Kann, D. A., Zeh, A., et al. 2006, *A&A*, **457**, 857  
 Fitzpatrick, E. L., Massa, D., Gordon, K. D., Bohlin, R., & Clayton, G. C. 2019, *ApJ*, **886**, 108  
 Foreman-Mackey, D., Hogg, D. W., Lang, D., & Goodman, J. 2013, *PASP*, **125**, 306  
 Freudling, W., Romaniello, M., Bramich, D. M., et al. 2013, *A&A*, **559**, A96  
 Fryer, C. L., Andrews, S., Even, W., Heger, A., & Safi-Harb, S. 2018, *ApJ*, **856**, 63  
 Fryer, C. L., Burns, E., Ho, A. Y. Q., et al. 2025, *ApJ*, **986**, 185  
 Fryer, C. L., & Kalogera, V. 2001, *ApJ*, **554**, 548  
 Georgy, C., Meynet, G., Walder, R., Folini, D., & Maeder, A. 2009, *A&A*, **502**, 611  
 Glennie, A., Jonker, P. G., Fender, R. P., Nagayama, T., & Pretorius, M. L. 2015, *MNRAS*, **450**, 3765  
 Gordon, K. 2024, *JOSS*, **9**, 7023  
 Gordon, K. D., Cartledge, S., & Clayton, G. C. 2009, *ApJ*, **705**, 1320  
 Gordon, K. D., Clayton, G. C., Declair, M., et al. 2023, *ApJ*, **950**, 86  
 Gordon, K. D., Fitzpatrick, E. L., Massa, D., et al. 2024, *ApJ*, **970**, 51

- Gordon, K. D., Misselt, K. A., Bouwman, J., et al. 2021, *ApJ*, **916**, 33
- Groot, P. J., Bloemen, S., Vreeswijk, P. M., et al. 2024, *PASP*, **136**, 115003
- Guevel, D., Hosseinzadeh, G., Bostroem, A., & Burke, C. J. 2021, *dguevel/PyZOGY: v0.0.2*, Zenodo, doi:10.5281/zenodo.4570234
- Gutiérrez, C. P., Mattila, S., Lundqvist, P., et al. 2024, *ApJ*, **977**, 162
- Gutiérrez, E. M., Bhattacharya, M., Radice, D., Murase, K., & Bernuzzi, S. 2025, *PhRvD*, **111**, 3031
- Hamidani, H., Ioka, K., Kashiyama, K., & Tanaka, M. 2025a, arXiv:2503.16242
- Hamidani, H., Sato, Y., Kashiyama, K., et al. 2025b, *ApJ*, **986**, 4
- Herant, M., Benz, W., Hix, W. R., Fryer, C. L., & Colgate, S. A. 1994, *ApJ*, **435**, 339
- Heywood, I., 2020 Oskat: Semi-automated Imaging of MeerKAT Observations, Astrophysics Source Code Library, ascl:2009.003
- Ho, A. Y. Q., Goldstein, D. A., Schulze, S., et al. 2019, *ApJ*, **887**, 169
- Ho, A. Y. Q., Kulkarni, S. R., Perley, D. A., et al. 2020a, *ApJ*, **902**, 86
- Ho, A. Y. Q., Margalit, B., Bremer, M., et al. 2022a, *ApJ*, **932**, 116
- Ho, A. Y. Q., Perley, D. A., Chen, P., et al. 2022b, *TNSAN*, **267**, 1
- Ho, A. Y. Q., Perley, D. A., Filippenko, A. V., et al. 2022c, *TNSAN*, **199**, 1
- Ho, A. Y. Q., Perley, D. A., Kulkarni, S. R., et al. 2020b, *ApJ*, **895**, 49
- Hugo, B. V., Perkins, S., Merry, B., Mauch, T., & Smirnov, O. M. 2022, in ASP Conf. Ser. 532, Astronomical Data Analysis Software and Systems XXX, ed. J. E. Ruiz, F. Pierfederici, & P. Teuben (San Francisco, CA: ASP), 541
- Izzo, L. 2025, *GCN*, **38912**, 1
- Izzo, L., Auchettl, K., Hjorth, J., et al. 2020, *A&A*, **639**, L11
- Izzo, L., de Ugarte Postigo, A., Maeda, K., et al. 2019, *Natur*, **565**, 324
- Jonas, J. 2018, in Proc. MeerKAT Science: On the Pathway to the SKA - PoS (MeerKAT2016), 277 (Trieste: SISSA), 001
- Jonker, P. G., Glennie, A., Heida, M., et al. 2013, *ApJ*, **779**, 14
- Kraft, R. P., Burrows, D. N., & Nousek, J. A. 1991, *ApJ*, **374**, 344
- Kumar, A., Maund, J. R., Sun, N. C., et al. 2025, *GCN*, **38907**, 1
- Levan, A. J., Cotter, L., Malesani, D. B., Martin-Carrillo, A., & Jonker, P. G. 2025a, *GCN*, **38909**, 1
- Levan, A. J., Jonker, P. G., Saccardi, A., et al. 2024, arXiv:2404.16350
- Levan, A. J., Rastinejad, J. C., Malesani, D. B., et al. 2025b, *GCN*, **38987**, 1
- Levan, A. J., Tanvir, N. R., Starling, R. L. C., et al. 2014, *ApJ*, **781**, 13
- Li, R. Z., Chen, X. L., Chatterjee, K., et al. 2025a, *GCN*, **38861**, 1
- Li, R. Z., Chen, X. L., Chatterjee, K., et al. 2025b, *GCN*, **38888**, 1
- Li, R. Z., Mao, J., Sun, H., et al. 2025c, *GCN*, **39037**, 1
- Li, W. X., Zhu, Z. P., Zou, X. Z., et al. 2025, arXiv:2504.17034
- Liang, E., Zhang, B., Virgili, F., & Dai, Z. G. 2007, *ApJ*, **662**, 1111
- Liu, X., An, J., Sun, N. C., et al. 2025a, *GCN*, **39583**, 1
- Liu, Y., Sun, H., Xu, D., et al. 2025b, *NatAs*, **9**, 564
- MacFadyen, A. I., & Woosley, S. E. 1999, *ApJ*, **524**, 262
- Malesani, D., Fynbo, J. P. U., Hjorth, J., et al. 2009, *ApJL*, **692**, L84
- Malesani, D. B., Levan, A. J., van Hoof, A., Jonker, P. G., & Xu, D. 2025, *GCN*, **38902**, 1
- Margalit, B. 2022, *ApJ*, **933**, 238
- Margutti, R., Metzger, B. D., Chornock, R., et al. 2019, *ApJ*, **872**, 18
- Masci, F. J., Laher, R. R., Rusholme, B., et al. 2019, *PASP*, **131**, 018003
- Masci, F. J., Laher, R. R., Rusholme, B., et al. 2023, arXiv:2305.16279
- Matthews, D., Margutti, R., Metzger, B. D., et al. 2023, *RNAAS*, **7**, 126
- Matzner, C. D., & McKee, C. F. 1999, *ApJL*, **526**, L109
- Mazzali, P. A., Valenti, S., Della Valle, M., et al. 2008, *Sci*, **321**, 1185
- Mirabal, N., Halpern, J. P., An, D., Thorstensen, J. R., & Terndrup, D. M. 2006, *ApJL*, **643**, L99
- Modjaz, M., Li, W., Butler, N., et al. 2009, *ApJ*, **702**, 226
- Modjaz, M., Liu, Y. Q., Bianco, F. B., & Graur, O. 2016, *ApJ*, **832**, 108
- Moskvitin, A. S., Spiridonova, O. I. & GRB follow-up Team 2025, *GCN*, **38925**, 1
- Nakar, E. 2015, *ApJ*, **807**, 172
- Nakar, E., & Piran, T. 2017, *ApJ*, **834**, 28
- Nasa High Energy Astrophysics Science Archive Research Center (Heasarc), 2014 HEASoft: Unified Release of FTOOLS and XANADU, Astrophysics Source Code Library, ascl:1408.004
- Nava, L., Salvaterra, R., Ghirlanda, G., et al. 2012, *MNRAS*, **421**, 1256
- Nicholl, M., Srivastav, S., Fulton, M. D., et al. 2023, *ApJL*, **954**, L28
- O'Connor, B., Pasham, D., Andreoni, I., et al. 2025, *ApJL*, **979**, L30
- Offringa, A. R., McKinley, B., Hurley-Walker, N., et al. 2014, *MNRAS*, **444**, 606
- Olivares, E. F., Greiner, J., Schady, P., et al. 2012, *A&A*, **539**, A76
- Page, K. L., Evans, P. A., DeLaunay, J. & Swift XRT Team 2025, *GCN*, **39584**, 1
- Patel, M., Gompertz, B. P., O'Brien, P. T., et al. 2023, *MNRAS*, **523**, 4923
- Perley, D. A., Ho, A. Y. Q., Yao, Y., et al. 2021, *MNRAS*, **508**, 5138
- Perley, D. A., Mazzali, P. A., Yan, L., et al. 2019, *MNRAS*, **484**, 1031
- Piro, A. L., Haynie, A., & Yao, Y. 2021, *ApJ*, **909**, 209
- Piro, A. L., & Kollmeier, J. A. 2018, *ApJ*, **855**, 103
- Planck Collaboration, Aghanim, N., Akrami, Y., et al. 2020, *A&A*, **641**, A6
- Prentice, S. J., Maguire, K., Smartt, S. J., et al. 2018, *ApJL*, **865**, L3
- Prochaska, J., Hennawi, J., Westfall, K., et al. 2020, *JOSS*, **5**, 2308
- Quirola-Vásquez, J., Bauer, F. E., Jonker, P. G., et al. 2022, *A&A*, **663**, A168
- Quirola-Vásquez, J., Bauer, F. E., Jonker, P. G., et al. 2023, *A&A*, **675**, A44
- Rastinejad, J. C., Levan, A. J., Jonker, P. G., et al. 2025, *ApJL*, **988**, L13
- Ravasio, M. E., Burns, E., Wilson-Hodge, C., Jonker, P. G. & Fermi-GBM Team 2025, *GCN*, **39146**, 1
- Rho, J., Evans, A., Geballe, T. R., et al. 2021, *ApJ*, **908**, 232
- Saccardi, A., Zhu, Z. P., Schneider, B., et al. 2025, *GCN*, **39585**, 1
- Sarin, N., Hübner, M., Omand, C. M. B., et al. 2024, *MNRAS*, **531**, 1203
- Schlaflly, E. F., & Finkbeiner, D. P. 2011, *ApJ*, **737**, 103
- Schroeder, G., Ho, A., & Perley, D. 2025, *GCN*, **38970**, 1
- Senno, N., Murase, K., & Mészáros, P. 2016, *PhRvD*, **93**, 083003
- Shilling, S. P. R. & Swift UVOT Team 2025, *GCN*, **39587**, 1
- Shingles, L., Smith, K. W., Young, D. R., et al. 2021, *TNSAN*, **7**, 1
- Smith, K. W., Smartt, S. J., Young, D. R., et al. 2020, *PASP*, **132**, 085002
- Soderberg, A. M., Kulkarni, S. R., Nakar, E., et al. 2006, *Natur*, **442**, 1014
- Soderberg, A. M., Berger, E., Page, K. L., et al. 2008, *Natur*, **453**, 469
- Sollerman, J., Jaunsen, A. O., Fynbo, J. P. U., et al. 2006, *A&A*, **454**, 503
- Song, F. F., Li, R. Z., Wang, B. T., et al. 2025, *GCN*, **38972**, 1
- Srinivasaragavan, G. P., Hamidani, H., Schroeder, G., et al. 2025, arXiv:2504.17516
- Srivastav, S., Chen, T. W., Gillanders, J. H., et al. 2025, *ApJL*, **978**, L21
- Steele, I. A., Smith, R. J., Rees, P. C., et al. 2004, *Proc. SPIE*, **5489**, 679
- Sun, H., Li, W. X., Liu, L. D., et al. 2025, *NatAs*, Advanced Online Publication
- Tan, J. C., Matzner, C. D., & McKee, C. F. 2001, *ApJ*, **551**, 946
- Team CASA, Bean, B., Bhatnagar, S., et al. 2022, *PASP*, **134**, 114501
- Thöne, C. C., de Ugarte Postigo, A., Fryer, C. L., et al. 2011, *Natur*, **480**, 72
- Toma, K., Ioka, K., Sakamoto, T., & Nakamura, T. 2007, *ApJ*, **659**, 1420
- Tonry, J. L., Denneau, L., Heinze, A. N., et al. 2018, *PASP*, **130**, 064505
- van Dalen, J. N. D., Levan, A. J., Jonker, P. G., et al. 2025, *ApJL*, **982**, L47
- Vernet, J., Dekker, H., D'Odorico, S., et al. 2011, *A&A*, **536**, A105
- Virgili, F. J., Liang, E.-W., & Zhang, B. 2009, *MNRAS*, **392**, 91
- Wang, H., Dastidar, R. G., Giannios, D., & Duffell, P. C. 2024, *ApJS*, **273**, 17
- Wang, L. J., Wang, X. F., Cano, Z., et al. 2019, *MNRAS*, **489**, 1110
- Whitesides, L., Lunnan, R., Kasliwal, M. M., et al. 2017, *ApJ*, **851**, 107
- Woosley, S. E. 1993, *ApJ*, **405**, 273
- Woosley, S. E., & Bloom, J. S. 2006, *ARA&A*, **44**, 507
- Woosley, S. E., Eastman, R. G., & Schmidt, B. P. 1999, *ApJ*, **516**, 788
- Xu, D., Zhu, Z. P., Liu, X., et al. 2025, *GCN*, **38984**, 1
- Yao, Y., Ho, A. Y. Q., Medvedev, P., et al. 2022, *ApJ*, **934**, 104
- Yin, Y.-H. I., Zhang, B.-B., Yang, J., et al. 2024, *ApJL*, **975**, L27
- Yuan, W., Zhang, C., Chen, Y., & Ling, Z. 2022, in Handbook of X-ray and Gamma-ray Astrophysics, ed. C. Bambi & A. Sanganello (Berlin: Springer), 86
- Zackay, B., Ofek, E. O., & Gal-Yam, A. 2016, *ApJ*, **830**, 27
- Zhang, W., Yuan, W., Ling, Z., et al. 2025, *SCPMA*, **68**, 219511
- Zheng, J.-H., Zhu, J.-P., Lu, W., & Zhang, B. 2025, *ApJ*, **985**, 21
- Zhu, Z. P., Liu, X., Fu, S. Y., et al. 2025a, *GCN*, **38885**, 1
- Zhu, Z. P., Corcoran, G., Levan, A. J., et al. 2025b, *GCN*, **38908**, 1
- Zou, X., Liu, C., Kumar, B., et al. 2025, *GCN*, **38914**, 1